Factors affecting the stability of perovskite solar cells: a comprehensive review

Unni Krishnan
Manjot Kaur
Manjeet Kumar
Akshay Kumar

SPIE.

Factors affecting the stability of perovskite solar cells: a comprehensive review

Unni Krishnan,[a] Manjot Kaur,[a] Manjeet Kumar,[b] and Akshay Kumar[a,*]

[a]Sri Guru Granth Sahib World University, Advanced Functional Materials Laboratory, Department of Nanotechnology, Fatehgarh Sahib, Punjab, India

[b]Incheon National University, Department of Electrical Engineering, Incheon, Republic of Korea

Abstract. Accelerated depletion of fossil fuel, energy demands, and pollution force us to choose renewable and eco-friendly energy resources. Solar cells are considered as an efficient replacement for fossil fuel. In the family of solar cells, silicon-based solar cells and perovskite solar cells (PSC) have displayed significant power conversion efficiency (PCE). Perovskites have been investigated extensively over the past two decades, due to their advantageous properties, such as high absorption coefficient, efficient carrier mobility, long charge diffusion length, and direct bandgap. These features make PSC a prospective candidate to replace silicon in solar cells. By 2018, PSC achieved an encouraging PCE of 23.3%. However, low stability and toxicity have retarded the commercialization of PSC. With the aim of assisting junior researchers, we consider the latest achievements in this domain and review the field from a stability and performance perspective. We emphasize recent developments and methodologies to overcome drawbacks concerning stability and toxicity. © *2019 Society of Photo-Optical Instrumentation Engineers (SPIE)* [DOI: 10.1117/1.JPE.9.021001]

1 Introduction

The survival of the human species on Earth is a function of human health, proper climatic conditions, and their affecting factors. Due to heavy energy demands, there has been an increase in the consumption of fossil fuel, which has elevated the pollution levels leading to global warming. Thus, the development of an alternate eco-friendly power source is vital to sustain the life on Earth. The global requirement of power is estimated to grow exponentially every year. Solar cells are considered as a promising way to meet these energy crises and reduce pollution.[1] Since the last few decades, a silicon-based solar cell acts as an ideal solution. The production of silicon-based solar cells has increased by 10 times from 2005 to 2013. Silicon-based solar cells have obstacles such as cost factor, complicated production procedure, and conversion efficiency far less than the optimum value. Perovskites solar cells (PSC), which have various technical advantages, are considered as a better replacement for silicon solar cells and have a high chance for commercialization. To avail this opportunity, PSC and their associated factors have been extensively investigated by researchers.

Currently, silicon-based solar cells have efficiencies over 15%. However, they have a high energy pay-back time and CO_2 emission rate.[2] Cost of module, balance of systems,[1] and operation management, though reducing, is reaching a stagnation value far below the optimum. These drawbacks have generated demands for exploration of new material with high-performance capability. The field of conversion of solar energy to electrical energy has experienced a substantial boost due to development of perovskite-based solar cells. The reported high efficiency of solid-state-sensitized thin film (solar cell based on perovskite CH_3NH_3PbI as light harvester)[3] has encouraged investigation in this domain. Figure 1 shows the increment in research papers published in the last few years on perovskites. This increased research
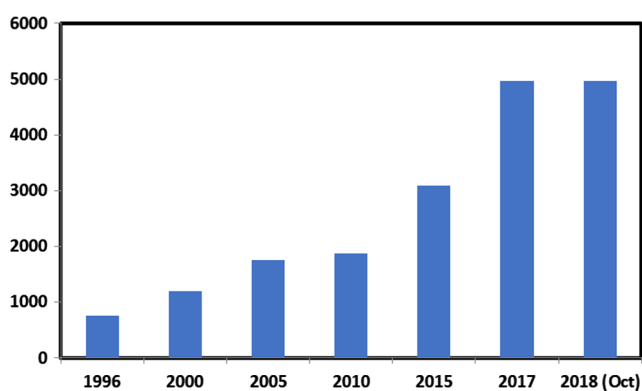

Fig. 1 Number of articles published per year on perovskites.[4]

Table 1 Development of various structure resulting in increase of efficiency.

Year	Device structure	PCE (%)	Reference
2018	As certified by NREL	23.3	5
2017	FTO/TiO$_2$/meso TiO$_2$: perovskite composite/perovskite /PTAA/Au	22.1	6
2016	FTO/bl-TiO$_2$/mp-TiO$_2$/Csx(MA$_{0.17}$FA$_{0.83}$)$_{(1-x)}$Pb($_{I0.83}$Br$_{0.17}$)$_3$/spiro-c	21.1	7
2015	FTO/bl-TiO$_2$/mp-TiO$_2$/(FAPbI$_3$)$_{1-x}$(MAPbBr$_3$)$_x$/PTAA/Au	20.1	8
2014	ITO-PEIE/Y-TiO$_2$/CH$_3$NH$_3$PbI$_{3-x}$Cl$_x$/spiro-OMeTAD/Au	19.3	9
2013	ITO/np-ZnO/CH$_3$NH$_3$PbI$_3$/spiro-OMeTAD/Ag	15.7	10
2013	FTO/graphene-TiO$_2$/mp-Al$_2$O$_3$/CH$_3$NH$_3$PbI$_{3-x}$Cl$_x$/OMeTAD/Au	15.6	11
2013	FTO/bl-TiO$_2$/mp-TiO$_2$/ CH$_3$NH$_3$PbI$_3$/spiro-OMeTAD/Au	15	12
2013	FTO/bl-TiO$_2$/mp-Al$_2$O$_3$/CH$_3$NH$_3$PbI$_{3-x}$Cl$_x$/spiro-MeTAD/Ag	12.3	13
2012	FTO/bl-TiO$_2$/mp-TiO$_2$/CH$_3$NH$_3$PbI$_3$/spiro-OMeTAD/Au	9	3
2011	FTO/bl-TiO$_2$/mp-TiO$_2$/CH$_3$NH$_3$PbI$_3$/redox liquid electrolyte/Pt	6.5	14
2009	FTO/bl-TiO$_2$/mp-TiO$_2$/CH$_3$NH$_3$PbI$_3$/redox liquid electrolyte/Pt	3.8	13

confirms that PSC has rapidly evolved as an answer to energy crises; presently (by 2018), it can achieve an efficiency of 23.3% (Table 1).[8,9,12,13,15–17] Further, the National Renewable Energy Laboratory (NREL) graph shows the rapid pace of increment in efficiency achieved in the last few years.[18]

Despite such aggressive progress, the contribution of solar cells, to meet the world's electricity requirement is less than 1%.[19] In solar cells, light-to-electricity conversion efficiency η is defined as a product of open circuit current density (J_{sc}), open circuit voltage (V_{oc}), and fill factor (FF). Research is going on to achieve power conversion efficiency (PCE) up to Shockley–Queisser limit, which is 33.5% for the single-junction solar cell.[20] Theoretical limits as calculated for a conventional PSC employing CH$_3$NH$_3$PbI$_{3-x}$Cl$_x$ absorber ($E_g \sim 1.55$ eV) are $J_{sc(SQ-limit)}$ is 27.20 (mA/cm^2), $V_{oc(SQ-limit)}$ is 1.28 V, FF$_{(SQ-limit)}$ is 90.2, and PCE$_{(SQ-limit)}$ is 31.4%.[21] However, actual results concerning PCE are limited to 15.4%. It has also drawbacks such as lead toxicity, low operational stability, and large-scale production issues. Recently, Christians et al. achieved operational stability of >1000 h, by tailoring the interfaces of PSC.[22] Although it is a positive sign, perovskites have to accomplish the levelized cost of electricity for residential use as 5.0 cents per kWh and achieve a stable lifespan of at least 20 years by 2030 to achieve successful commercialization.[23] Production of 1 kWh of energy from perovskites would incur
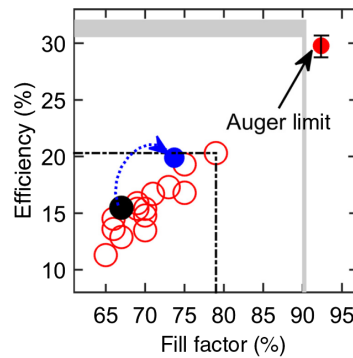
Fig. 2 Performance trends of recently reported PSCs (shown by open circles). Shaded region shows a detailed balance limits (with only radiative recombination) for FF and efficiency. Red dot with error bar shows a detailed balance limit in presence of Auger recombination. Error bars correspond to an order of magnitude change in Auger recombination coefficient. Blue dotted curve and the solid circle indicate possible performance improvement. Reprinted with permission from Ref. 25. © 2015, AIP Publishing.

a consumption of 64.77% embodied energy and 31.38% of incorporated materials. This wastage of energy and materials assures that there is enormous room for improvement.[24] Figure 2 shows the blue-dotted curve and a solid circle, which indicates the scope for performance improvement.[25] The following four conditions would enable a solar cell to maximize its power output.

- Obey Maxwell–Boltzmann statistics and exhibit a mobility of charge carrier sufficiently high reaching as high as a 10 cm^2 V^{-1} s^{-1}.[26]
- Radiative band-to-band recombination. Radiative efficiency from band-to-band transition for PSC is higher than organic solar cells.[26,27]
- Internal conversion efficiency reaches 100%.
- Photon recycling effect occurs in the cell.[27–31]

CH$_3$NH$_3$PbX$_3$ (where X denotes I and Br) with a band gap of 1.5 to 2.3 eV,[32] close to optimum gap, shows the best performance in PSC. The success of hybrid PSC is due to the properties of organic and inorganic components in it. Organic elements render stability for perovskites and facilitate self-assembly, whereas inorganic component produces extended meshwork by covalence and ionic interactions. This hybrid combination and their interactions allow precise crystalline structure formation. Efficient carrier mobility, (multi) ferroics,[33,34] high absorption coefficient (5.7 × 10^4 cm^{-1} at 600 nm), long charge diffusion length,[35–38] low nonradiative Auger recombination,[39] and direct band gap properties define good performance and efficiency of perovskite. In addition, Perovskite materials show a strong PL with a narrow full width at half maximum.[40,41]

CaTiO$_3$ is the original perovskite mineral, which was discovered and named after Russian mineralogist Lev Perovski. In 1978, Dieter Weber was the first to show hybrid perovskites. They initially explored lead halide and later tin, bromide, and iodide. Incidentally, they did not incorporate any improvements as they considered it as another semiconductor. Perovskites started their journey as light absorbers in dye-sensitized solar cells (DSSC). O'Regan and Grätzel reported fabricating DSSC by use of a nanoscopic titanium dioxide (TiO$_2$) particle layer achieving PCE of 7.1%.[42] PCE of a different PSC structure ranges from 17% to 20.1% (9.3% for single junction,[43] 20.1% for regular structure, 19% for planar heterojunction, 21.6% for mesoporous, 17% for planar heterojunction, and 18% for inverted planar heterojunction). New metal halide perovskite films were fabricated by a single step method utilizing a molar ratio of 1.05 between PbI$_2$/formamidinium Iodine, providing efficiency of 20.8%.[44] These films are used in light-emitting diodes,[45,46] solution-processed photodetectors,[47–49] and lasers.[50] Transition metal oxide perovskites, such as LaVO$_3$ (mott insulators) displays an indirect band gap of 1.08 eV. The **d–d** transitions and **p-d** transitions ensure adequate absorption and utilization in solar cells.[51] Heterostructures, such as LaVO$_3$ grown on SrTiO$_3$ with a direct band gap of 1.1 eV, are also

investigated for higher PCE solar cells.[52] Doped perovskite solar cell (PSC) gained importance, especially with hetrovalaent elements. Their energy states can be tuned and reported to achieve PCE of 15.6% (0.956 sun, AM 1.5).[53] Roldan-Carmona et al.[54] fabricated semitransparent thin PSC films that maintained near to device transparency of 30% and PCE above 6%.

2 Structure

First perovskite material $CaTiO_3$, with a general formula AMX_3, is called perovskite. All perovskites are not solar perovskite structured compounds. Figure 3 shows an ideal structure of perovskite. The "A" cation represents methylammonium cations ($CH_3NH_3^+$), M represents heavy metal cation, and "X" is a halogen—chlorine, bromine, iodine, or combination of three.[56] The schematic structure of an ideal perovskite is shown in Fig. 4.[55] $CH_3NH_3PbI_3$ has a distorted three-dimensional (3-D) structure that crystallizes in the tetragonal I4/mcm space group.

Lead methylammonium iodide perovskites can have three crystalline phases, which are temperature-dependent, namely orthorhombic, tetragonal, and cubic. An extensive investigation is on for control of metal halide hybrid structure from 3-D to two-dimensional (2-D),[57,58] one-dimensional (1-D),[59] and 0D with quantum confinement. Figures 5 and 6 show the XRD pattern and FESEM morphological image of conventional $CH_3NH_3PbI_3$ perovskite film, respectively, against different thermal annealing temperature ranging from 80°C, to 140°C.[60] XRD pattern confirms the presence of perovskite with peaks at 2θ values of 14.2 deg (110), 28.5 deg (220), and 31.8 deg (310). The peak at 12.7 represents PbI_2 phase. Unlike $CH_3NH_3PbI_3$, which has a distorted tetragonal crystal, $CH_3NH_3PbBr_3$ has a cubic perovskite structure phase of $Pm\bar{3}m$ space group at room temperature, along with variation in their energy levels as shown in Fig. 7.[61]

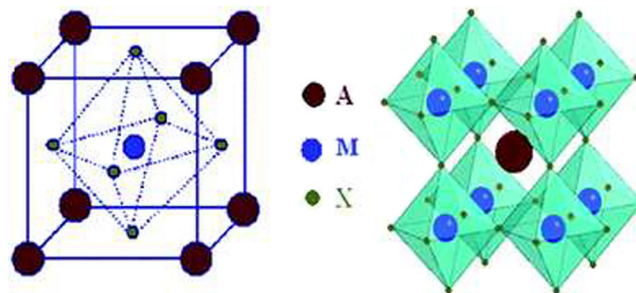**Fig. 3** General perovskite structure. Reprinted with permission from Ref. 55. © 2010 by the Royal Society of Chemistry.
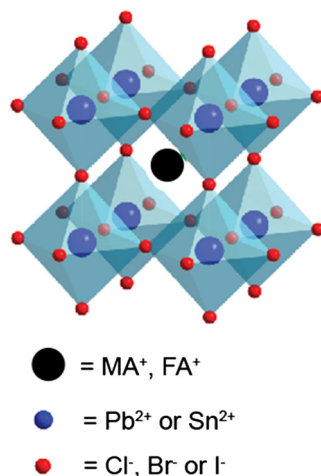

= MA⁺, FA⁺

= Pb²⁺ or Sn²⁺

= Cl⁻, Br⁻ or I⁻

Fig. 4 Crystal structure of iodide perovskite $CH_3NH_3PbI_3$, consisting of three ions: methylammonium (MA), lead, and iodine.

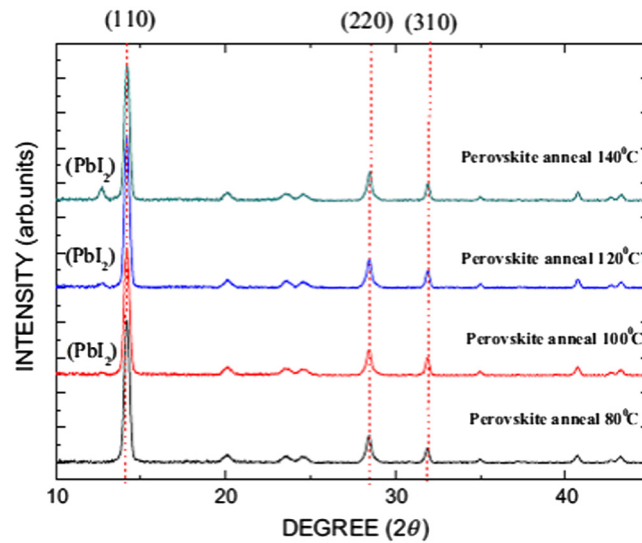**Fig. 5** XRD diffractograms of $CH_3NH_3PbI_3$ perovskite film after different thermal annealing temperatures. Reprinted with permission from Ref. 60. © 2015 by Elsevier.
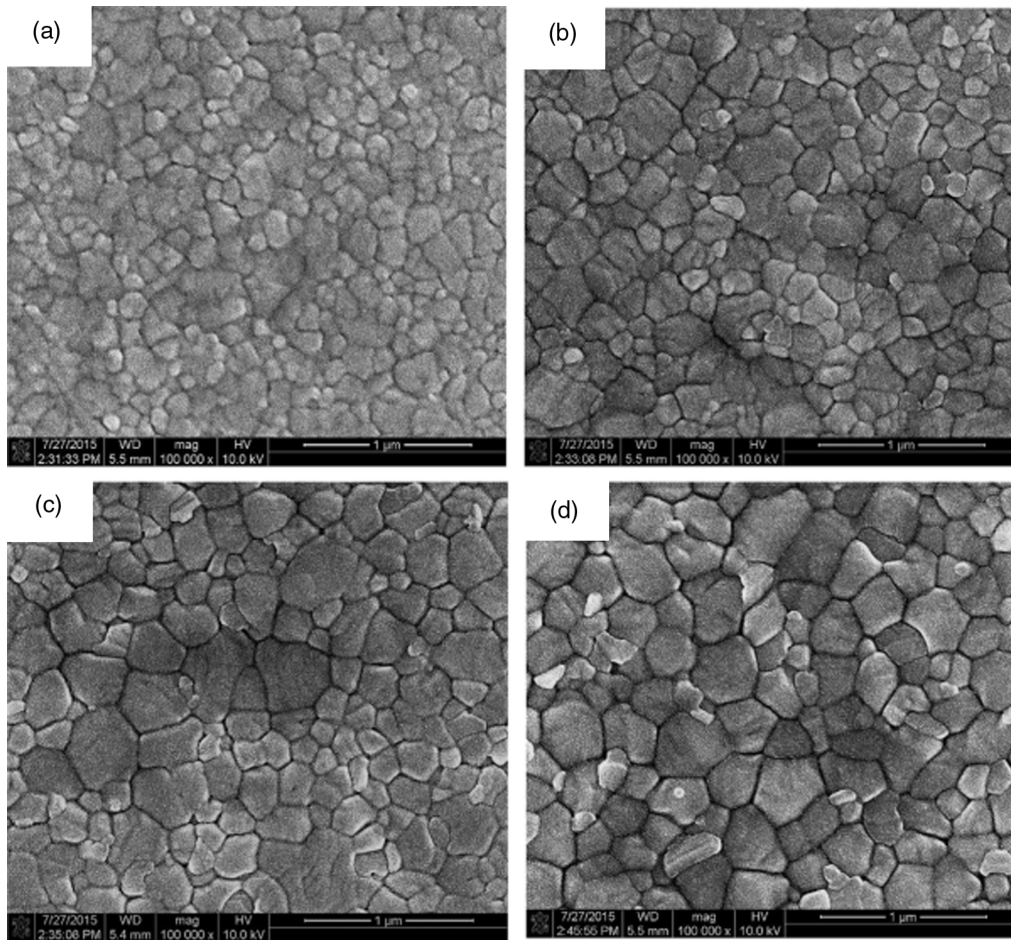

Fig. 6 FESEM morphological image of perovskite film. (a) Thermal annealing to 80°C. (b) Thermal annealing to 100°C. (c) Thermal annealing to 120°C. (d) Thermal annealing to 140°C. Reprinted with permission from Ref. 60. © 2015 by Elsevier.
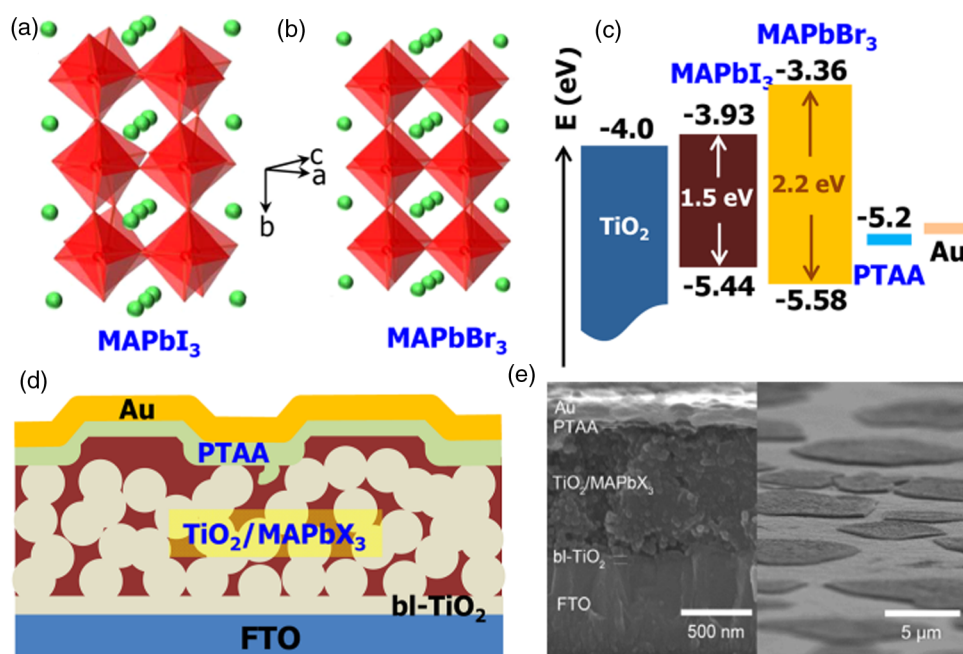
Fig. 7 (a) Distorted tetragonal crystal structures of $MAPbI_3$ at room temperature. (b) Cubic perovskite structure of $MAPbBr_3$. Red: polyhederon $[PbX_{6/2}] - (X = I, Br)$; green sphere: $CH_3NH_3 (= MA)$. (c) Conduction band minimum and valence band maximum of $MAPbI_3$, $MAPbBr_3$, and TiO_2 are represented in eV. (d) Device configuration of the hybrid heterojunction solar cell consisting of FTO/(bl-TiO_2)/TiO_2/$MAPbX_3$ bilayer nanocomposites/PTAA/Au layer. (e) FESEM images, in cross sectional view, displaying different layers in the real device. Reprinted with permission from Ref. 61. © 2013 by the American Chemical Society.

In addition, research for fabricating hybrid PSC with various organic cations and metal halide anions is on.

New structures such as double perovskites ($A_2B^IB^{III}X_6$), replace Pb^{2+} with nontoxic trivalent/monovalent metals, are reported to yield high efficiency.[62] The family of PSC constitutes structures such as dye-sensitized cells, mesoporous structure, planar (p-i-n and n-i-p) structure, HTL and ETL free cells, flexible cells, and tandem cells. The prominent structures of solar cells are as follows.

2.1 Mesoporous Structured Solar Cell

Mesoporous structured solar cell (MSSC) is a third-generation device with low fabrication cost. TiO_2 is the most common mesoporous layer in them. Though TiO_2 nanoparticles are the most commonly used in the mesoporous layer, success reports are available while employing TiO_2 nanosheets,[63] nanorods, and nanofibers. MSSC consists of a single-phase triple-conducting oxide (TCO), blocking layer, mesoporous TiO_2 or Al_2O_3 scaffold, perovskite absorber, hole transport layer (HTL), and a metal electrode in its construction (Fig. 8).[64] Usually, MSSC fabrication done by a two-step deposition method. The processing temperature is in the range of 150°C. However, highly efficient MSSC devices have a high sintering temperature of 500°C.[65] During high-temperature sintering, the mesoporous layer allows rapid extraction of photo-induced electrons, which shorten the electron transport length. This shortening of length makes MSSC an efficient light harvester. However, they suffer from the various disadvantage of having low open-circuit voltage (V_{oc}) and lower light absorbance at wavelengths greater than 700 nm. Mesoporous Al_2O_3, which acts as an insulator, is found to be more stable than TiO_2, under continuous illumination. TiO_2 introduces nonstoichiometry defects, such as titanium interstitials and oxygen vacancies, which causes trap sites.[66] Encapsulation of layers can prevent moisture ingress and degradation. Etgar et al.[63] recently reported that spin-casting a methylammonium lead iodide ($CH_3NH_3PbI_3$) solution on a 400-nm thick TiO_2 nanosheet would form a mesoscopic ($CH_3NH_3PbI_3$)/TiO_2 heterojunction. Evaporating a gold film on top of
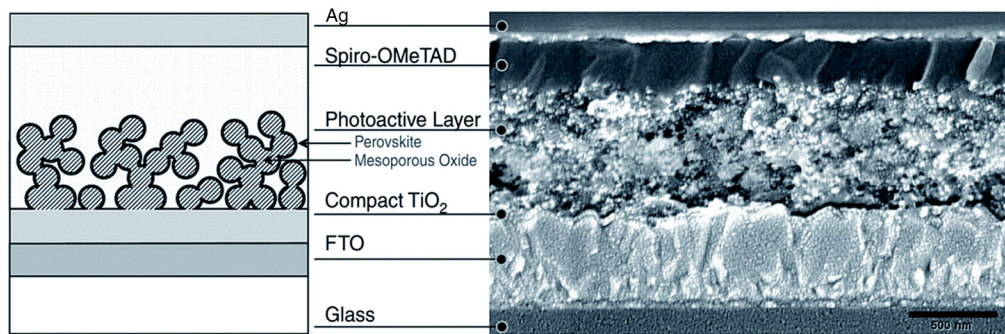
Fig. 8 Schematic illustrating of mesoporous PSCs. The mesoporous oxide can be an electron transporting semiconductors, such as TiO_2, ZnO, or an insulating layer, such as Al_2O_3 or ZrO_2 (MSSC). Reprinted with permission from Ref. 64. © 2012 by the American Association for the Advancement of Science.

$CH_3NH_3PbI_3$ creates a back contact. It provided PCE of 5.5%, short circuit photocurrent $J_{sc} = 16.1$ mA/cm^2, and open-circuit photovoltage $V_{oc} = 0.631$ V under Am 1.5 solar light of 1000 W/m.[63]

2.2 Planar Structure

Film structure has a simple construction as it does not have a mesoporous scaffold or electronic layer in it, facilitating ease in fabrication. Figure 9 shows the architecture of n-i-p and p-i-n variants with different location of the charge transport layer, which is their primary difference.[67] A simple planar junction designed between perovskite and HTM layer, without scaffolding, corresponds to a simple planar thin-film cell. The major problem in the fabrication of this structure is to avoid contact between HTM and blocking layer. Vapor deposition and dual-source vapor method excel in achieving this required feature. Docampo et al.[68] applied NiO_x and VO_x in planar heterojunction solar cells with $CH_3NH_3PbI_{3-x}Cl_x$ as photoactive material. However, these NiO_x and VO_x interlayers resulted in low photovoltaic performance due to poor coverage on the substrate by perovskite film.[68] Alternatively, UV treatment was reported to enhance surface wetting properties with increased PCE by 7% on these materials. HCl improves crystallization and coverage of PbI_2 in thin film, which subsequently improves the morphology achieving a PCE of 14.8% for perovskite thin film.[69] Planar heterojunction additionally assists in evaluating and testing of the new materials and their effect, for solar cell fabrication. SnO_2 was also experimented to replace TiO_2 as electron-selective contact. SnO_2 was
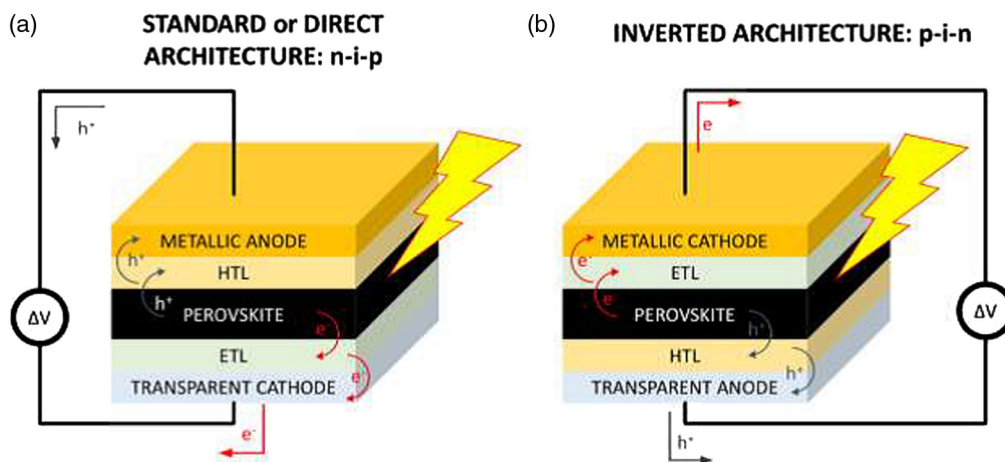

Fig. 9 Schematic representation of two different configurations used PSC. (a) Standard architecture n-i-p and (b) inverted architecture p-i-n. Reprinted with permission from Ref. 67. © 2017 by Elsevier.

spin coated and sintered at a much lower temperature of 200°C than TiO_2. Its fabrication included the solvent vapor annealing, which crystallizes the residual PbI_2 and adds it at the interface of $SnO_2/CH_3NH_3PbI_3$. PSC devices based on SnO_2 displayed high stability of holding the PCE of 13% till 700 h.[70]

2.3 HTL/ETL Free Cells

The fundamental task of any photovoltaic device is to create charge carriers, i.e., holes and electrons on the absorption of light energy. Further separating them at respective heterojunction and making them available at their respective electrodes. This separation depends on energy offsets versus exciton binding energy. It defines the formation of two primary interfaces, perovskite/electron transport layer (ETL) interface and perovskite/HTL interface. The architecture of a few PSCs does not have HTL or ETL layers. As these are not mandatory layers, numerous researchers have developed PSC without HTL[71,72] or ETL with good PCE. Perovskite layer has Au deposited over it while fabricating the HTL-free PSC. In this, perovskite layer conducts the duty of absorber and hole conductor by forming a heterojunction with ETL. Aharon et al.[71] have reported a two-step deposition method to fabricate highly optimized HTL-free PSC with a PCE of 10.85%, FF of 68%, and V_{oc} of 0.84 V. Their performance is strongly dependent
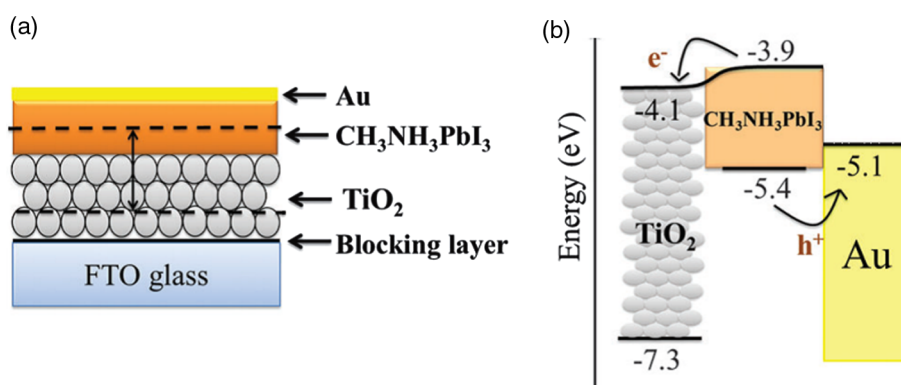
Fig. 10 (a) Structure of hole conductor free $TiO_2 - CH_3NH_3PbI_3$ perovskite-based solar cells. Arrow indicates the depletion region observed at $TiO_2 - CH_3NH_3PbI_3$ junction. Reprinted with permission from Ref. 71. Copyright (2014) Royal Society of Chemistry. (b) Energy level diagram that shows charge separation process. The position of energy levels is taken from Ref. 63. © 2012 American Chemical Society.
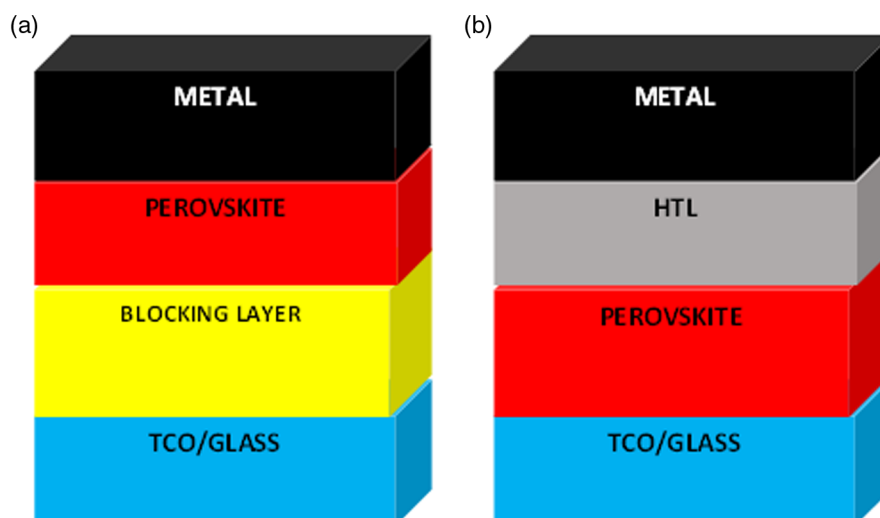
Fig. 11 Structure of PSC: (a) HTL-free PSC and (b) ETL-free PSC.

on the width of the depletion layer formed by TiO_2-$CH_3NH_3PbI_3$. Depletion layer supports charge separation and restricts back reaction from TiO_2 to $CH_3NH_3PbI_3$. The width of the depletion layer is evaluated using Mott Schottky analysis.[73] Figure 10 shows a schematic diagram of HTL-free PSC with their energy levels.[71] Figure 11(b) shows ETL-free PSC in-which an insulator (Al_2O_3) replaces TiO_2 scaffold,[64] which proves that perovskite material could effectively transport electrons without an ETL. Production cost for HTL-less cells is high, leading to an increase in device cost. Further, the presence of the HTL layer complicates the mechanism followed for extraction.

2.4 *Tandem Cells*

Tandem cells consist of two formats, i.e., four-terminal and two-terminal devices. Figure 12 shows the arrangement of four-terminal tandem device, which has two-terminal devices/ cells. They are either mechanically stacked or monolithically integrated through tunneling junction. Baillie and his coworkers[74] with copper indium gallium selenide, Asadpour et al.[75] with a highly efficient a-Si:H/c-Si heterojunction bottom cell and Mailoa et al. using the c-Si bottom cell on perovskite/silicon multijunction solar cell have obtained PCE of 30%, 13.4%, and 13.7%, respectively. Due to the limitation of band gap mismatch and current matching constraints, a traditional tandem cell of Si and perovskites could only achieve PCE of 24% and 20%, respectively. Top cell absorbs high energy photons and bottom cell harness the remaining low-level energy photons. $MAPbI_3$ makes an excellent top layer in c-Si solar cells. Hydrogenated indium oxide, having high mobility, is used as a rear electrode to fabricate semitransparent PSCs.[76] Fabrication of two-terminal tandem solar cells with perovskite as the top layer and kesterite copper zinc tin sulfide (CZTS) as bottom cells was reported to attain a PCE of only 4.6%. This reduction is primarily due to semitransparency of the top aluminum electrode, resulting in transmission loss.[77] Thus, the highly efficient and transparent top layer is a very critical factor. Further, they should be immune to thermal instability and hygroscopicity. Numerous transparent electrodes used here are ultrathin metal such as Au,[78] graphene,[79] carbon nanotubes,[80] and Ag nanowires.[19] However, efficiency achieved was below 10%, and their contacts featured strong absorption in near-infrared (NIR). PSC that are individually efficient underperformed when used as tandem cells, due to sensitivity to a thickness of perovskite layer. Thus, bifacial tandem cell
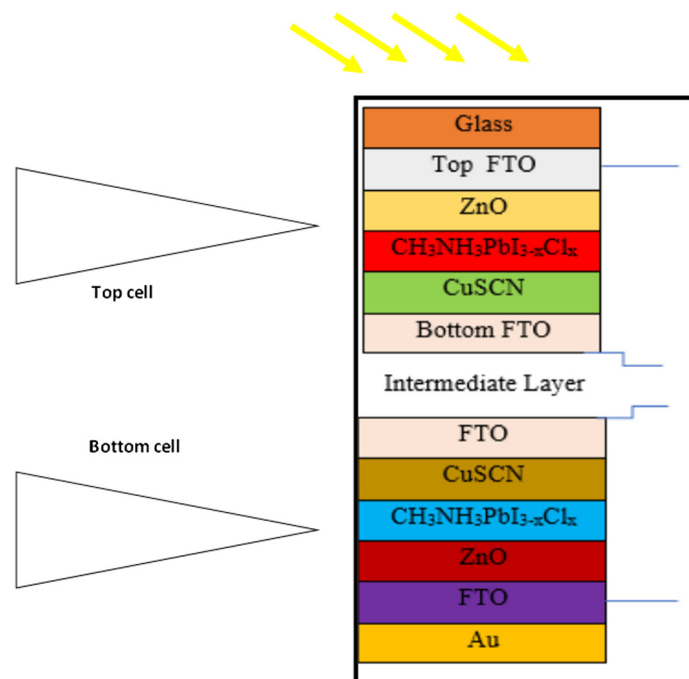

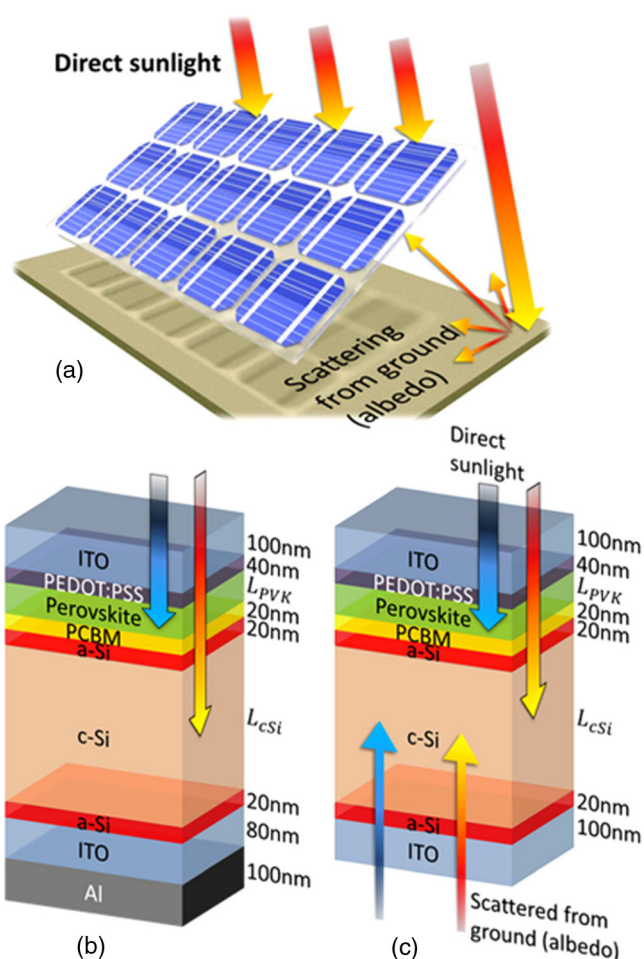**Fig. 12** Architecture of a four-terminal PSC.

Fig. 13 (a) Operational bifacial tandem solar panel, utilizing direct illumination of sunlight and a fraction of light that scatters from the ground onto back of the panel. (b) Traditional tandem structure and (c) a bifacial tandem structure. Reprinted with permission from Ref. 75. © 2015, AIP Publishing.

was fabricated, which utilizes scattered light back from the ground (Fig. 13) to achieve a PCE of ~33%.[75] Further, they are immune to variations in perovskites layer thickness.

3 Fabrication

Fabrication is a prominent factor in PSC. Fabrication factors such as time, solvent mixtures, doping, and humidity have a marked effect on crystallization of perovskites.[81] Further processing routes and solvents selected induce intermediate phases and influence device performance with film quality.[81] Synthesis and analysis protocol for large-scale production and laboratory analysis are different. Most of the PSC that achieved high efficiency in the lab, on small devices, does not possess commercialization advantage. Large-scale production of PSC should be cost-effective, good stability, and maintain high performance. Figure 14 shows a one-step and two-step spin coating method. The perovskites precursor solution is thoroughly stirred and dropped on to the substrate and accelerated for evaporation of the solvent.[83] In the second step, crystalline perovskites are achieved, after thermal annealing the sample, by removing the residual solvent. $CH_3NH_3PbI_3$ or $CH_3NH_3PbI_{3-x}Cl_x$ when fabricated by spin coating led to the formation of scattered nanodots[3] and extremely thin layer.[64] General drawbacks such as poor quality film, small grain sizes, and dense pinholes can be controlled to a limited extent by additive engineering[84,85] to obtain required grain sizes. This process has achieved a maximum PCE of 19.19%. Another major drawback of spin coating is the formation of nonuniform thickness
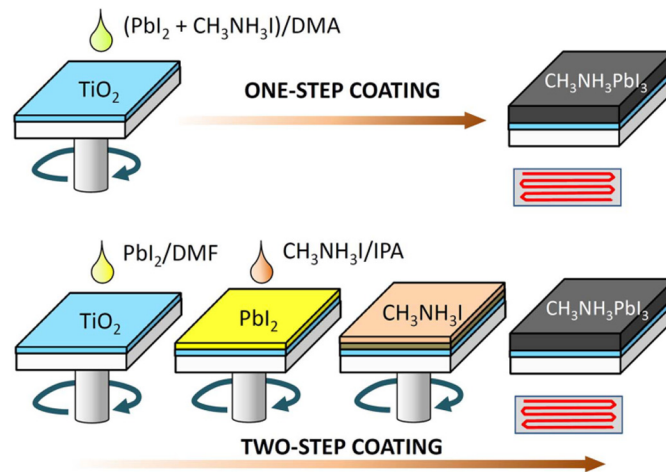
Fig. 14 One-step and two-step spin-coating procedures for $CH_3NH_3PbI_3$ formation[82] used in accordance with the Creative Commons Attribution (CC BY) license.

of the film from center to edges. Two-step coating provides full coverage of PbI_2 with cube-like structure.[82]

Two-step spin-coated deposition method, as a valid mode for fabrication of PSC, was reported in 2013. It involves step-by-step spin coating of PbI_2 solution and solution of methylammonium iodide (MAI) on the substrate. Whole set up is thermally annealed at 100°C driving the interdiffusion of precursors. Single step method produces uncontrolled precipitation of perovskite, resulting in large morphological variations, which hampers the prospects for practical applications. Thus, in performance sequential deposition process,[12] PbX_2 solution is first spin-coated on top of the substrate and then is dipped into a solution of MAI. The performance gets varied according to different soaking time, from 5 s to 2 h. The optimum soaking period was found to be 15 min, which resulted in enhancement of current density and voltage of the device from 10.1 mA/cm^2 and 933 mV (5 s) to 15.1 mA/cm^2 and 1036 mV (15 min),[86] respectively. This method can perform successfully for nanostructured devices with planar heterojunction structured PSC.

The sequential vapor deposition process is very similar to the two-step spin coating method except that this method uses vapor deposition, which yields layered multistack thin films over large areas.[17] MAI and PbI_2 were vapor deposited on a substrate as layers before thermal annealing. Yang and his coworkers used vapor-assisted solution process (VASP), also called a blended deposition method, to produce MAPbI$_3$ films as shown in Fig. 15.[87] A solution of PbI_2 in N,N-dimethylformamide was deposited on the substrate by spin coat method. Later, PbI_2-coated substrate is annealed in MAI vapor at 150°C in a nitrogen atmosphere for the desired time to yield perovskite films. Though spin-coating techniques offer good thin film uniformity for lab-scale experiments, its drawbacks are concerning wastage of solution during coating, unsuitable for large-scale production, and low material transfer efficiency. However, vacuum and solution processes are two primary methods to fabricate perovskite films starting with inorganic and organic counterparts of PSC. Solution process results in the rough film surface. Vacuum process requires high energy for creation of vacuum conditions, and the flaky nature of MAI powder makes synthesis less controllable. VASP resulted in enhanced controllability of film quality. VASP method takes advantage of the characteristics of the hybrid nature of perovskite materials, particularly the low sublimation temperature of organic halides and fast reaction rate between inorganic and organic species. Full surface coverage, 100% precursor transformation, uniform grain structure, and print size up to 2 μm are highlights of perovskite film derived from this approach. It is free of pinhole defects and yields an efficiency of 15.4%.[17] Snaith and his coworkers synthesized PSC using dual-source vacuum deposition method. In this process, MAI and $PbCl_2$ were preheated to 120°C and 325°C, respectively, and evaporated together using separate sources, to attain superior uniformity in films.[17] Vapor-based deposition
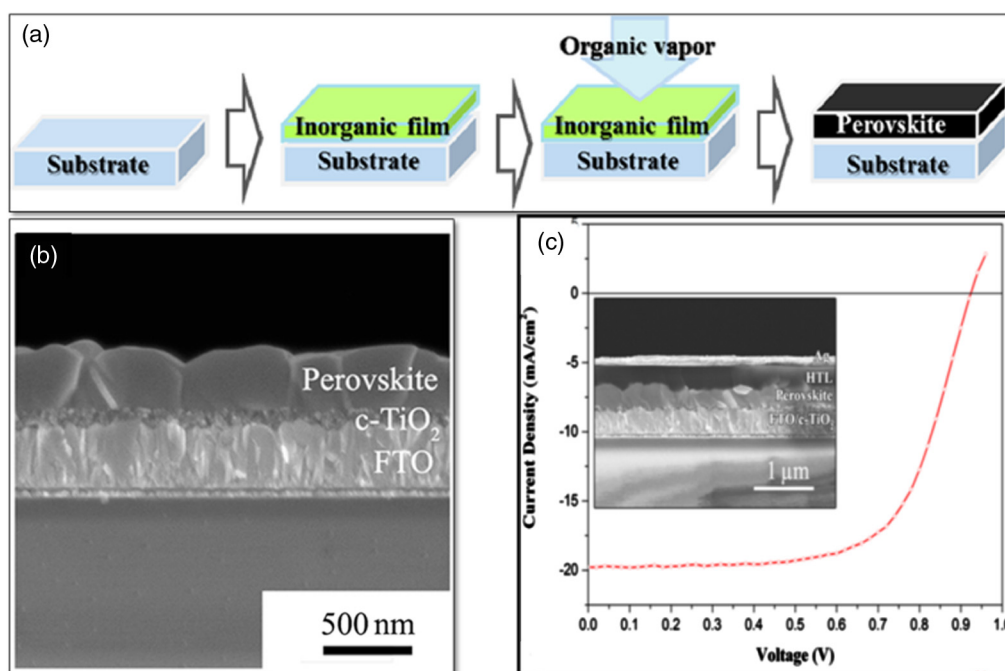
Fig. 15 (a) Schematic Illustration of perovskite film formation through VASP, (b) cross-sectional SEM image, (c) current density–voltage (*J*–*V*) characteristics of the solar cell based on the as-prepared perovskite films under AM 1.5G illumination, and cross-sectional SEM image of the device (inset). Reprinted with permission from Ref. 87. © 2013 by the American Chemical Society.

processes have few issues in comparison to solution-based deposition processes, such as an increase in manufacturing cost and capability to achieve increased efficiencies.[88,89]

Analysis showed that large crystal would have a noticeable effect on PCE, leading to the development of hot-casting technique. This method guarantees large output and ultrafast production.[90] In this, precursor (iodide) is maintained at 70°C and is immediately transferred to spin coater as drops in less than 5 s. Rotating for 30 s assists in cooling and quenching it fast, results in a uniform film with large grain size. Figure 16 shows a schematic diagram of the hot casting process and displays the proportional relation between temperature and large grain formation. Figure 16(d) shows a comparative chart of grain size and processing temperature for the hot-casting method and conventional annealing method.[91] The comparison confirms that the evaporation rate defines the formation of larger crystals. In 2015, Vak's group have fabricated a fully printed planar-heterojunction PSC by slot-die coating.[92,93]

Large-scale perovskites production for roll-to-roll fabrication consisted of various methods, such as slot-die coating, knife coating, spray coating, screen printing, gravure printing, flexographic printing, and inkjet printing.[94] Slot-die is a premetered coating process, in which mass flow determines the thickness of the film. Metered solution feed controls the formation of a uniform thickness of film stripes. In addition, transferring the complete solution to the substrate would lead to zero loss of solvent. This process involves two steps. The first step consists of heating the substrate at 70°C, which results in dense and glassy PbI_2.[12,94] The second approach replicates the quenching mechanism to avoid large crystals. It consists of high-pressure nitrogen flow allowing layers to dry faster. Spray coating and doctor blading are few methods that are advantageous when integrated with the roll-to-roll process. The genesis of spray coating is from polymer solar cell fabrication.[95] It is combined with ultrasonic spray to enable large-scale production in room temperature. PSC achieved a PCE of 13% with 0.065 cm^2 active area on glass substrates[96] by this method. Spray coating is reported to be a favorable method for fabricating tandem structural devices and mixed cation halide perovskites for achieving enhanced performance and stability.[97] It utilizes minimum solid concentration for large-scale production but has
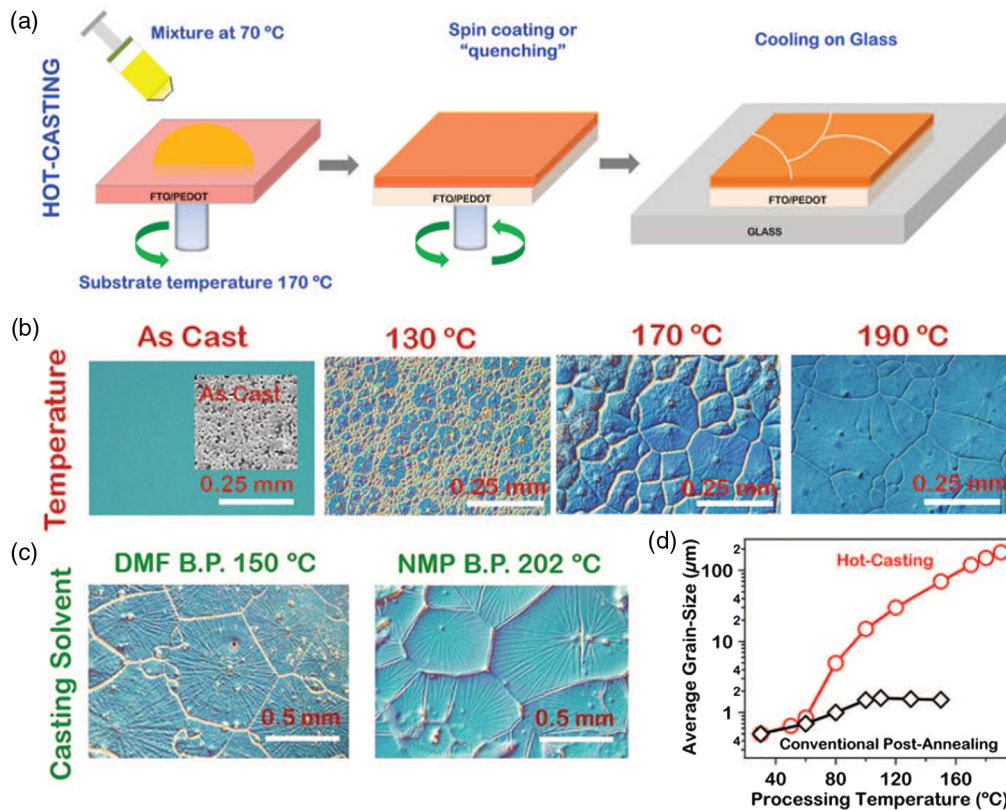
Fig. 16 (a) Hot-casting method and (b) optical micrographs of grain formation as a function of substrate temperature with casting solution maintained at 70°C. (c) Large area grain formation using casting solvents with high boiling points. (d) Comparison of grain size as a function of processing temperature obtained for the hot-casting and conventional postannealing. Reprinted with permission from Ref. 91. © 2015 by the American Association for the Advancement of Science.

a disadvantage of excessive restrictions on boiling points of solvents used. Inkjet process is programmable production process but has limitations induced due to ink properties.[98]

Doctor blading method has an advantage of slower evaporation time, cost-efficient, higher coverage area, better crystal quality, nil solution waste, and favorable for ambient temperature processing.[99] It is reported to be highly compatible with the roll-to-roll production process for optoelectronic device fabrication.[92,100,101] By applying blade coating for preparation of $CH_3NH_3PbI_{3-x}Cl_x$ perovskite films, under ambient conditions, yields large crystalline domains, high quality, and moisture/air-resistant films. Slower evaporation time leads to better quality crystals and higher coverage. For perovskites, the formation of large crystalline domains is encouraged by a relatively slow solvent drying process, on the uniformly wet film formed by solution blading.[102,103]

4 Stability

Stability and degradation though have different meaning; they together define the issues and parameters, which affect existence, availability, and commercialization of PSC. Stability of PSC is our concern, as they degrade significantly after a few hundred hours of usage. Even after the necessary coating, they can sustain only 80% of initial efficiency after 500 h. Performance and efficiency of PSCs decrease, as degradation increases with time. Evaluation of stability is as per standard of International Electrotechnical Commission damp heat test (at 85°C, 85% relative humidity). Stable devices can maintain its performance with less than 10% reduction of PCE after 1000 h of exposure.[104,105] Hybrid PSCs are still struggling to reach this goal. Significant
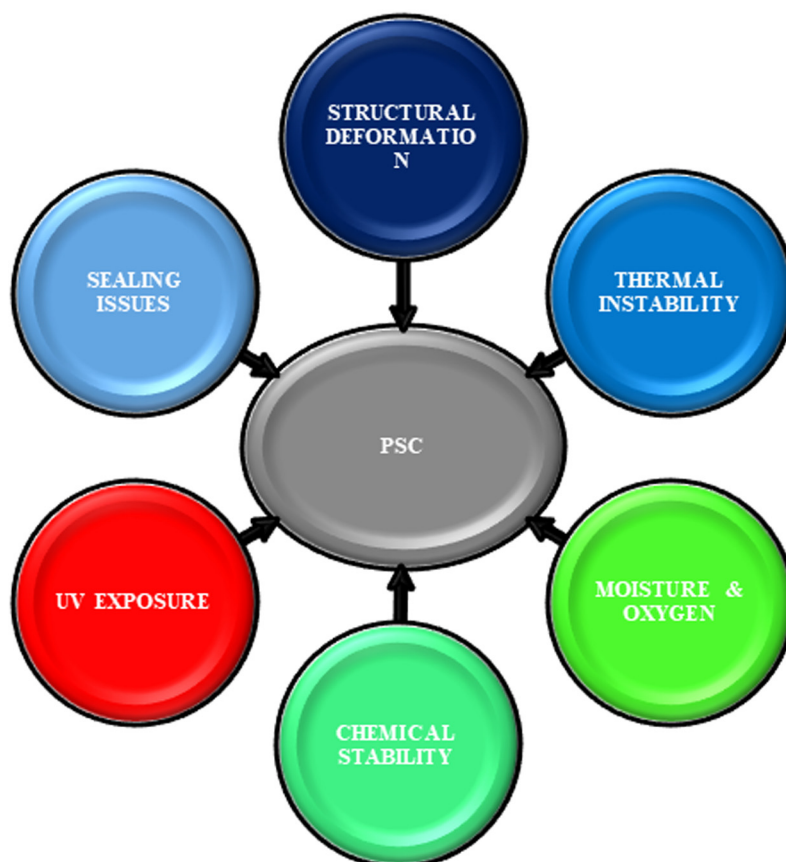
Fig. 17 Factors affecting stability of PSC.

factors affecting stability are sensitivity to moisture, ultraviolet exposure, thermal stress, and so forth. (Fig. 17).[106,107] In addition, a prominent hurdle for commercialization of PSC is toxicity and safety issues due to lead usage.[108] Optimum fabrication method for large-scale production of PSC is still under research. Material instability can be regulated utilizing cross-linking additives and compositional engineering.[109] The best example is adding a combination of $Pb(CH_3CO_2)_2$ $3H_2O$ and $PbCl_2$ in precursors,[110] additionally using cation cascade, including Cs and Rb cations.[7,111] Associated layers of PSC induce instability into PSC. Monitoring of deterioration by different performance parameters, such as J_{sc}, V_{oc}, FF, and η, describe its stability status. Fabrication processes, light absorption, charge separation, charge carriers transport mechanisms of different layers influence performance parameters. Table 2 shows various methodologies undertaken to increase the stability factor. Unlike organic solar cells, the decay behavior of V_{oc} in hybrid PSC, $CH_3NH_3PbI_3$, follows three steps. These three steps are a fast partial decay within 10 to 100 μs, followed by an extremely slow decay between 1 and 100 ms, and then a final rapid decay on the 10-s timescale.[130] Initial decay is continuous until 70% and holds at that sector for a hybrid PSC, whereas an organic solar cell decays very fast, within 1 s.

Half-life is the time required to reach half of the initial absorbance in set conditions. It determines the strength of decomposition, mainly due to RH. For RH of 98%, 80%, 50%, and 20%, the half-life of $MAPbI_3$-based PSC films are estimated to be 4, 34, 1000, and 10,000 h, respectively. The half-life is found to be independent of film depth confirming that moisture diffuses into the bottom of the PSC layer along the grain boundaries.[131] Methodology for evaluating stability is also an essential factor. Researchers at Aalto University have found that only a fraction of stability tests done on perovskite-based solar cells and DSSCs meet proper requirements.[132] The team analyzed 261 aging tests, conducted on solar cells, and saw significant shortcomings in the procedure of reporting test results and testing methodology. These defects emphasized the importance of standardization of testing methodology. Presently, tests are

Table 2 Methodologies to increase stability of PSC.

Architecture	Type	Methodology	η (%)	Stability check result	Other advantages	References
Glass/FTO/c-TiO$_2$/m-TiO$_2$/H$_3$PbI$_3$/carbon	Hole conductor free	P-type NiO nanoparticles into carbon electrodes	13.26	Retained 85% of initial efficiency after 800 h in ambient atmosphere.	Easy electron transfer	112
FTO/TiO$_2$/MAPbI$_3$/HTM/Au(HTM = acylhydrazone-based porphyrin derivative)	Planar	Acylhydrazone-based porphyrin derivative used as HTM layer	17.8	Retained 65% of the initial PCE after 60 h for water stability. Maintained original PCE after 100 h for thermal stability.	Improved water stability with contact angles of water droplets at ~107°C	113
Graphene/AU/spiro-OMeTAD/TiO$_2$/perovskite/ZnO-MgO-EA$^+$/FTO	Planar and mesoporous	Surface passivation of ZnO by a thin layer of MgO and protonated ethanolamine (EA)	22.1	Stable in air for more than 300 h are achieved when graphene is used to further encapsulate the cells at AM 1.5G illumination and 70% RH	No hysteresis	114
FTO/ALD-NiO/Cs$_{0.05}$MA$_{0.95}$PbI$_3$/PCBM/BCP/ALD-AZO/Ag	Inverted PSC	Al-doped ZnO films act as efficient electron-transporting	18.45	Retains 86.7% of initial PSC for 500 h under 1 Sun illumination at 85°C	Negligible current–voltage hysteresis in this work	115
FTO/mesoscopic ZrO$_2$/TiO$_2$ infiltrated with /(5-aminovaleric acid)$_x$(MA)$_{1-x}$PbI$_3$	Mesoporous	Uses a double layer of mesoporous TiO$_2$ and ZNO	12.8	Near to initial PCE at AM 1.5 sunlight over 1008 h at room temperature	Hole-conducting layer is eliminated	116
Al/PCBM/2-D (BA)$_2$(MA)$_3$Pb$_4$I$_{13}$//poly(3,4-ethylenedioxythiophene)polystyrene sulfonate (PEDOT:PSS))/FTO-glass	Planar	Ruddlesden–Popper phases-layered 2-D perovskite films	4.73	Unencapsulated, it retains >60% efficiency for 2250 h under AM1.5G at 65% RH	Photovoltaic efficiency of 12.52%, no hysteresis, no deterioration when encapsulated	117
Fluorine-doped tin-oxide (FTO) /bl-TiO$_2$/mp-TiO$_2$/(FAPbI$_3$)$_{0.95}$(MAPbBr$_3$)$_{0.05}$/HTM/Au.	Film/planar	Fluorene-terminated hole-transporting material		High thermal stability maintaining almost 95% of its initial performance for >500 h at 60°C	High glass transition temperature average grain size suitable for electron extraction	118
FTO/polytriarylamine (PTAA)/Cs$_{0.05}$ MA$_{0.16}$ FA$_{0.79}$ Pb(I$_{0.83}$Br$_{0.17}$)$_3$/C (unsealed)	Planar	Stress modulation to increase stability		Stress of −130 to 130 MPa after 24 h of damp air aging at 25°C and 85% RH	Compressive load increases stability	119

Table 2 (*Continued*).

Architecture	Type	Methodology	η (%)	Stability check result	Other advantages	References
FTO/NixMg$_{1-x}$ LiO/MAPbI$_3$/PCBM/Ti(Nb)O$_x$/Ag (sealed)	Inverted planar	p-doped (p$^+$) NixMg$_{1-x}$O and n-doped (n+) TiO$_x$	>15	Retained 90% of PCE at AM 1.5 G, 100 mW/cm^2, 1000 h	No hysteresis	16
Glass/NDI-(P(NDI2DT-TTCN)/PEDOT: PSS/CH$_3$NH$_3$PbI$_3$/ITO/glass	Inverted PSC	Naphthalene diimide (NDI)-based polymer along with dicyanothiophene (P(NDI2DT-TTCN)) used as ETL	17	Deteriorated less than PSC with PCBM at 25°C under ~55% of RH for 100 h	Electron extraction ability forming a hydrophobic ETL surface. Excellent mechanical stability negligible hysteresis	120
Al/PC$_{61}$BEH/CH$_3$NH$_3$PbI$_3$/PEDOT:PSS/ ITO	Inverted planar	Fullerene derivative with branched alkyl chain such as [6,6]-phenyl-C$_{61}$, butyric acid 2-ethylhexyl ester (PC$_{61}$BEH) as ETLs	15.19	Under AM 1.5G irradiation 45% to 50% humidity in air at room temperature without encapsulation		121
Glass/FTO/m-MTDATA/MAPbI$_3$/C$_{60}$/ BCP/Cu	Inverted planar	4,4′,4″-tris(N-3-methylphenyl-N-phenylamino) triphenylamine (m-MTDATA) as HTM layer	18.12	Retains 90% PCE in ambient temperature 30% RH for 1000 h.	Small hysteresis, large recombination resistance. Good water resistance and hydrophobicity with water contact angle of 83°C	122
ITO/SnO$_2$/MAPbI$_3$/spiro-OMeTAD/Ag (unsealed)	Planar	SnO$_2$ layer as electron selective contact prepared by sinter-less spin-coating processes	13	PEC constant over 700 h at AM 1.5 G.	Grain size of PbI$_2$ precursors can be controlled good thermal stability	70
ITO/TiO$_2$-Cl/(Cs$_{0.02}$FA$_{0.98}$PbI$_3$)$_{0.97}$ (MAPbBr$_3$)$_{0.03}$/spiro-OMeTAD/Au	Film	Perovskite seeding growth (PSG) method for Cs-containing, high-quality FAPbI$_3$-based PSC	21.5	Retain 60% of their initial efficiency after 140 h under one sun illumination.		123

Table 2 (*Continued*).

Architecture	Type	Methodology	η (%)	Stability check result	Other advantages	References
ITO/PEDOT:PSS/FA$_{0.75}$Cs$_{0.25}$Sn$_{0.5}$Pb$_{0.5}$I$_3$/C$_{60}$/BCP/Ag	Two terminal tandem solar cells	Tin content at 50% or below, using formamidinium and cesium at the A-site, and employing the postdeposition methylammonium chloride (MACl) vapor treatment	19.1	Unencapsulated maintains full PCE after 150 h at 85°Cover 80% of its initial PCE for over 300 h	Small bandgap PSC, low-cost, encapsulation technologies will be sufficient to prevent oxidation	124
Ag/spiro-OMeTAD/perovskites/MesoTiO$_2$ and perovskites compact TiO$_2$/FTO	3-D perovskite film	Distinct layered low-dimensional perovskite is engineered on top of the 3-D film	20.1	Retains 85% of initial PCE when subjected to one sun illumination for 800 h at 50°C	Negligible hysteresis, increased charge recombination resistance	125
TO/NiO$_x$/CH$_3$NH$_3$PbI$_3$/PCBM:C$_{60}$/Zr:acac/Ag	p-i-n film	Post-device ligand treatment. Stitching effect	20.13	Unencapsulation 70% PCE maintained under ambient conditions after a 500-h maximum-power-point tracking test	Healing and improves PCE to 900%	126
Au/spiro-OMeTAD/2-D@3-D perovksite/mp-TiO$_2$/c-TiO$_2$/FTO	2-D/3-D perovskites	Highly oriented 2-D@3-D [(AVA)$_2$PbI$_4$@MAPbI$_3$] perovskite structure combining	18.0	Device stability under inert is 90% of initial PCE for 32 days. Unencapsulated, retains 72% of initial PCE for 20 days under ambient conditions	Moisture stability at RH of ≈ 93%. Combines advantages of 2-D and 3-D perovskites	127
Al/PCBM/ZnO.np/Cs$_{0.05}$(MA$_{0.17}$FA$_{0.83}$)$_{0.95}$Pb(I$_{0.9}$Br$_{0.1}$)$_3$/NiO$_x$np/substrate/ITO	Flexible inverted PSCs	NiO$_x$ nanoparticles as HTL and ZnO nanoparticles as ETL	18.6	Over 85% of PCE is retained after 1000 h for thin film and over 90% after 500 h with a thick films.	Good stack development with negligible hysteresis	128
Cs$_x$FA$_{1-x}$PbI$_3$-[GaAA3]4(0 < x < 1)	Core/shell heterostructure	Gallium(III) acetylacetonate (GaAA3) as the precursor additive to *in situ* induce a metal–organic-complex monomolecular intermediate ([GaAA3]4)	18.24	Unencapsulated cell retains constant PCE over 18% for 5 h at 50% RH	Shows low defect-state density, strong luminescence and long lifetime of photogeneration charge carriers	129

conducted only on one cell and in dark region only.[132] Many reports state that samples that are stable in humid conditions were found to be unstable in UV light.[132] Only 15 tests conducted outdoors and three with cells connected, leading to erroneous results; checks need to be undertaken in real-world conditions in groups of several cells to bring in standardization.[132] The same team has developed a new method, which saves time, effort, and could assess deterioration to the smallest range. PSC solar films, when they get heated, they turn from black to lead iodide color, which is yellow, displaying degradation. This degradation does not happen in its bulk form, due to the catalytic activity of moisture and reduced surface area as compared to films.[132] PSC can be protected from moisture to a certain extent using PMMA [poly(methylmethacrylate)]. It also helps in nucleation and formation of smooth and fine films.[133] The next section discusses various direct and indirect factors that affect stability.

4.1 Structure

Materials and structure are also essential factors that decides the stability of PSC. The mesoporous structure formed by TiO_2-, Al_2O_3-, or ZrO-coated substrates, exhibited the pore-filling problem, low stability, and degraded performance.[17,64] Alteration of precursor influences the loss of organic material in PSC. This mass loss was reported to be 16%, 12%, and 5%, between temperatures of 250°C and 400°C[134] in three steps. Under sunlight and device operating temperature (~327°K), $CH_3NH_3PbI_3$ undergoes a phase transition from tetragonal to cubic. A disordered character is shown by methylammonium ions during the cubic–tetragonal transition, whereas PbX_6 octahedron displays a displacive character.[135,136] Various combinations of halogens, especially of Pb and Br, induce change and transformation in the crystal structure of $CH_3NH_3Pb(I_{1-x}Br_x)$. As x changes from 0 to 0.13, crystal structure transforms from tetragonal to cubic form with a change in the band gap. Empherical representation by quadratic equation $E_g(x) = 1.57 + 0.39x + 0.33x^2$ describes the dependence of band gap on x.[61] The low value of bowing parameter, 0.33, in the equation confirms high miscibility[137,138] of $MAPbI_3$ and $MAPbBr_3$. This low value shows that $MAPb(I_{1-x}Br_x)_3$ would constitute the entire composition of the compound and enables convenient band gap tailoring. For subservient Br fraction ($x < 2.0$), PCE remained unchanged with improved stability factor when tested for 20 days at 55% RH. Diminished cross-section and transformation from tetragonal to cubic stage, due to higher Br content, has led to enhanced stability.

New materials such as $CH_3NH_3SnI_3$ can resolve lead toxicity problems. Whole fabrication was conducted in N_2 environment as it decolorizes if exposed to the room environment. This decolorization is primarily due to oxidation of Sn^{2+} ions, which lead to the formation of oxides of Sn and residual perovskites material. Sn-based PSC shows an enhanced PCE of more than 6% and has a short diffusion length. It restricts the fabrication of devices with planar architecture. A combination of Sn with other halides, namely $CH_3NH_3Sn(I_{3-x}Br_x)$ was developed to achieve PCE of 6%.[139] Schoonman has explained the degradation in the absence of moisture.[140] Crystal structure of 3-D perovskites incorporating corner-sharing PbI_6 octahedra is broken into 1-D double chains consisting of two adjacent octahedral ($MAPbI_3 \cdot H_2O$, monohydrate form) and subsequently into 0D isolated octahedral ($MA_4PbI_6 \cdot 2H_2O$, dihydrate form) by intercalation of $H_2O[4]$. Structural degradation occurs due to ionization-simulated degradation; it happens when the hole of halide member, which the inner layers produce, migrates and reacts with negative iodine on the surface. The reports confirm that doping improves crystallization. GeO_2 doping, in planar PSC forming PEDOT:PSS-GeO_2 composite films, displayed active sites for crystal nucleus during annealing.[141] Doping has an overwhelming influence on performance, due to various reasons. Primarily it is due to undesired band bending at ETL and HTL interfaces with perovskites, increase in Auger recombination, and traps/defects. For higher PCE, the Fermi level in perovskite should not be above (below) Fermi level of ETL (HTL) in equilibrium.[25]

4.2 Materials of PSC

Perovskite materials exhibit features such as direct band gap, high optical extinction coefficients (10^4 to 10^5 cm^{-1}) in the NIR-visible region, and high carrier mobility ($\mu \sim 1$ to 10 cm^2 V^{-1} s^{-1}) making it a prospective member for light harvesting. A high optical extinction coefficient of

perovskite makes it a good absorption of light, at low mesoporous film thickness. Tuning the band gap of perovskite materials is achieved by modifying the chemical composition of perovskite[61] or by alloying different perovskites.[142] In addition to other properties, perovskite materials also exhibit ambipolar charge transport property (can be n- or p-type), which conducts electrons and holes through them, due to small effective mass of both electrons.[36,143–145] High dielectric constant leads to effective charge screening. By bandgap engineering through modification of the chemical composition of PSC, such as $CH_3NH_3PbI_{1-x}Br_x$, the entire spectrum is utilized.[146] Enhancement in PCE happens due to reduction in binding energy. The same was confirmed by incorporating core-shell Au_2SiO_2 in PSC and achieved PCE of 11.4%, $J_{sc} = 16.91$ mA/cm^2).[146] On addition of PbI_2, Sn halide perovskite exhibits photovoltaic properties. It attained a maximum photon to current conversion of 4.18% with 1060-nm-thick Sn layer, with a redshift at Sn thickness of 260 nm.[142] Variation in prominent layers and adaptation of methodology can increase stability and PCE. Addition of 5% by volume of water into MAI solution of isopropyl alcohol assists in preferential crystallization in (110) plane, achieving a large grain size of ~600 nm. This method achieved a PCE of 12.42%.[147]

4.2.1 *Electron conducting material layer*

A layer that supports electron transport and aids in avoiding hole-electron recombination is called ECM. LUMO level should be lower than the conduction band of perovskites to achieve high electron transfer, and for perfect hole blocking HOMO, should be below perovskites. Thus, normal ETM in $CH_3NH_3PbI_3$ perovskites will have LUMO of -3.9 eV and HOMO of -5.4 eV. TiO_2 is the most established and favorite ECM layer. It is highly photocatalytic in the UV regime and thus is a prime member in inducing instability due to UV exposure.[148] It provides a high surface area to perovskites loading and can exist with all nanostructures of 1-D, 2-D, and 3-D variants. Compact-TiO_2 results in lower PCE; however, ethanolamine (EA)-based solvent treatment of compact-TiO_2 would enhance the transport feature along with its defects. EA and ionic liquid molecules (ILMs) are spin coated on compact-TiO_2 modifying surface morphology of a planar perovskites.[149] Various other useful solvents that reduce defects of metal oxide and energy barrier mismatch are conjugated polyelectrolyte,[150] ILMs,[151] a self-assembled monolayer,[152,153] polar solvents, or alcohol/water-soluble-conjugated polymers.[154,155] TiO_2 is unsuitable on flexible substrates and large-scale production due to high sintering temperature.[64] ZnO, organic materials such as [6,6]-phenyl-C_{61}-butyric acid methyl ester (PCBM), and ICBA (indene C_{60} bis adduct), as well as carbon nanoforms and polymers, are an equivalent replacement of TiO_2 with good performance data.[156,157] Nanostructured ZnO in PSC can be fabricated at a low temperature (<150°C), making it viable for photovoltaic devices.[10] It has good electron mobility along with energy alignment. However, ZnO nanostructured, quadruple the rate of degradation due to deprotonation reaction of the organic part in perovskite.[158] PCE of 17.2% and enhancement of 23.2% compared to a nonadditive solution was observed by addition of non-halogen additives such as acetate (CH_3COO^-, Ac-) salts (NH_4Ac, NaAc) in CH_3NH_3I solution.[159] Modification of ZnO layer using ILMs, such as 1-benzyl-3-methylimidazolium chloride (benmim-Cl),[151] elevates performance. Further, TiO_2 is doped with various metals to overcome drawbacks. SnO_2 was experimented to replace TiO_2 as ECM material to achieve a high PCE of 13%.[70] In few devices, the TiO_2 layer is between Al anode and fullerene C_{60} for ensuring proper electronic contacts. Further research has led to the formation of valence bands of lower binding energies, with Fermi levels, within the band gap, by inserting a C_{60} monolayer between perovskite and TiO_2 contacts.[160] The ability of C_{60} to accept electrons results in high PCE, of 6.7%, along with enhancement of V_{oc} and J_{sc}. Planar devices using C_{60} as ETM and NiO as HTM achieved a PCE of 9.6%. For polymer ETM, solubility is a major issue. Thus, polymer ETM deposition will affect performance and perovskites layer. In addition to C_{60}, other ETM example consists of higher fullerene-like C_{70}, $PC_{71}BM$. Fullerene C_{60} and its derivative have increased PCE from 7.3% to 14.9% due to reduced trap density and lower degree of symmetry. However, due to nonequivalent double bonds, it leads to regioisomeric mixtures, which are difficult to separate -TiO_2 nanocomposites, as ETM, achieved PCE of 15.6%. Graphene quantum dots, due to their confinement in 3-D modify the band gap. Thus, incorporating these between TiO_2 and perovskites achieved PCE of 10.2% with a V_{oc} of 0.94 V and J_{sc} of 1.71 mA/cm^2.

4.2.2 *Hole conducting material layer*

The primary function of HTM is to extract charges selectively from perovskite and its interface. The basic advantage of this HCM is its ability to penetrate in mesoporous layer easily. However, it induces degradation in PSC film.[161] Classification of HCM consists of small molecules, polymers, and inorganics. Small molecule HCM such as spiro-OMeTAD is a favorite for mesoporous and planar structured PSC. Electrolytes have an inbuilt problem of low ionic conductivity. HTM is less conductive than perovskite material ($\sim 10^{-3}$ S cm^{-1}), leading to the requirement of thick HTM layer. High thickness is necessary to avoid pinholes and leakage, but in devices, it would lead to high series resistance and imbalance between series and shunt resistance. Thus, spiro-OMeTAD as solid-state HCM is introduced to nullify these limitations. However, multiplex synthetic approach and purification are the hindrances for its commercialization. Doping with lithiumbisimide (trifluoromethanesulfonyl) salt (LiTFSI), 4-tert-butylpyridine (TBP) and cobalt complex[162] assists in improving its conductivity. Due to absorption, device instability increases and oxidized form of spiro-OMeTAD starts acting as a filter in the visible region at 520 nm.[163] Spiro-OMeTAD shows an immediate initial decrease of 20% and, further, it declines steadily. New materials nicknamed EH44 are replacing spiro-OMeTAD, as it repels water and does not contain lithium.[164] PEDOT:PSS is another proven organic HTL for planar structured devices. There is energy level misalignment between PEDOT: PSS and VB (5.0 eV) of MAPbI$_3$ (5.46 eV), which results in lower V_{oc} (0.80 V). A higher work function of HTL would lead to strong recombination at the grain boundary, very low PCE, and affect the V_{oc} of the device. Doping and addition of additives were used to remove the misalignment and increase efficiency. Improved HTL doping ratio of 4:1 in volume for PEDOT:PSS-GeO$_2$ has achieved PCE of 15.15%, J_{SC} of 21.55 mA/cm^2, V_{oc} of 0.96 V, and FF of 0.74 under 100 mW/cm^2 AM 1.5 illumination.[141] MoO$_2$ nanoparticles/toluene solution an inorganic hole transporting material for planar CH$_3$NH$_3$PbI$_3$ PSCs is reported to exhibit stable efficiency of 14.8% under illumination of 1 Sun (100 mW/cm^2).[165] Numerous reports conclude NiO as a good candidate for HTM in PSC device fabrication. It was able to achieve PCE of 16.40% with high V_{oc} (1.04 V) and FF (0.72) with negligible current-voltage hysteresis.[166] The conjunction of mesoporous TiO$_2$ film and a hole conducting polymer led to the formation of PSC having 123% PCE under 1.5 Am.[158] CuSCN as HTM, along with a buffer layer of thin mesoporous alumina (Al$_2$O$_3$) and an added coat of insulating polymethyl methacrylate on PSC, was utilized to achieve PCE of 13.3%. In addition, it displayed stability by retaining the efficiency of 77% after 1000 h at 85℃ in air.[161] Utilization of bifunctional polymer nanocomposites as HTLs [CH$_3$NH$_3$PbI$_{(3-x)}$Cl$_x$] for light harvesting is also recently investigated with positive results. A gold (Au) nanoparticle assists in attaining a fourfold enhancement of electrical conductivity and carrier mobility. Scattering effects of doped nanoparticles have led to a 25% improvement in PCE along with amplification of the photon absorption on the photoactive layer.[167]

4.2.3 *Blocking layer*

Efficient lead halide PSCs use hole-blocking layers to help collection of photogenerated electrons and to achieve high open-circuit voltages. Deactivation of reactions at the surface of TiO$_2$ enhances stability, which is due to the blocking effect of this layer. Spiro-OMeTAD as HTL and TBP as additives to HTL would develop a reduction of perovskites film absorption. Introduction of montmorillonite layer between the perovskite and spiro-OMeTAD layers, as buffer, provides the solution for reduction in film absorption.[168] Experiments showed that nonencapsulated devices had higher stability than encapsulated devices because oxygen would remove the surface states and ensuring better stability.[66] Thus, oxygen is necessary for these devices. When Al$_2$O$_3$ replaces n-type TiO$_2$, as an insulating layer in MSSC, devices achieve stability of 1000 h.[169] Performance enhancement occurs when a hole-blocking layer is formed by Mg-doped TiO$_2$, with a PCE of 12.28%; high FF and V_{oc} (1.08 V). This enhancement is due to the enlargement of the gap between valence band and conduction band for better optical transmission properties.[170] Ke et al. have fabricated PSC without blocking layers, by growing perovskite directly in fluorine-doped tin oxide-coated.[171] Solution method and ultraviolet–ozone treatment can form layers. Its planar architecture consists of Au/hole-transporting material/

$CH_3NH_3PbI_{3-x}Cl_x$/substrate. It achieved a PCE of 14% and V_{oc} of 1.06 V, which is at par with conventional PSC. This success is due to ultraviolet–ozone treatment and involvement of Cl in synthesis. These results confirm that TiO_2 is not an ultimate interfacial material for achieving high-performance PSCs.[171]

4.2.4 Electrode

Electrode design for large-scale production is still a challenge. The electrode should ensure good catalytic activity, electron conduction, and high proton diffusion rates. A single-phase TCO is reported to have enhanced proton and charge transport capability for perovskites.[141] Ag and Au are the favorite elements.[172,173] However, due to the cost factor, Ag is a better alternative than Au.[146] However, PSC with Ag as electrode has extremely low stability. Exposure of element to humidity (RH ~ 50%) led to the formation of AgI, which deteriorates PCE. AgI transforms the electrode from a reflective metal to yellow color, which is highly influenced by the HTL layer. Antireflection coatings for front side of the transparent glass and plastic substrates are being explored extensively.[174–177] Nanophotonic front and rear electrodes for improved light transmittance in the solar cell is desirable for long wavelengths range operation in tandem device PSC. Successful nanopatterns are being replicated into transparent substrates for large-scale applications at low cost.[178] Long-term performance is a function of thermal stability of perovskite other layers in a photovoltaic device. Inorganic blocking layer and scaffold layer display appreciable stability compared to organic material in devices.

4.3 Hysteresis

Around 2014, scientists observed hysteretic current–voltage behavior of PSC.[179,180] Hysteresis, which is a specific property, is formed likely due to slow transient effects, leading to an over or underestimation of solar cell efficiency. $J–V$ hysteresis property of PSC is a function of dielectric response of perovskite material, mobile ions,[181] and trap-state discharging.[179] The shape of measured current–voltage (IV) curves and efficiency are function of scan direction, light source, delay in measurement time, and voltage bias conditions before measurement. It was established by various modeling and experimentation that hysteresis is weak when surface recombination is low and diffusion length is long.[182] Improved crystallinity, better fabrication process, and improved contacts are going to continue to improve hysteresis. HTMs influence hysteresis and $J–V$ curve. Cu-based, CZTS HTM express less hysteresis than with spiro-MeOTAD HTM.[183] $J–V$ hysteretic behavior of CuI-based devices with an efficiency of 7.5% is better than spiro-OMeTAD devices. Faster polarization relaxation was observed using EIS and OCVD for CuI-based devices.[184] Recently, in addition to normal-type of hysteresis, an inverted hysteresis that exhibits an opposite behavior to the normal is also reported.[185,186] The inverted hysteresis is due to interfacial charge extraction barriers formed by ionic defect accumulation and space charge build-up.[187] The inverted hysteresis is noted to be a function of bias range and sweep rate. Different bias scanning conditions lead to a varying ionic movement at the interface of the ETH or HTL/perovskite, which assists in the tuning of these hysteresis.[186]

Deposition of fullerene layers onto perovskites, which assists in the elimination of photocurrent hysteresis, is reported.[188] Methodology and accuracy for evaluating performance characteristics of PSCs are crucial. Hysteresis influences the evaluation of performance parameters such as $I–V$ curves and P_{max}. Measurement conditions such as sweep direction, start voltage, end voltage, hold time, and sweep time have an overwhelming effect.[189] Inverted devices (p-i-n structured) are reported to have less hysteresis.[182] Figure 18 shows that normalized time-dependent J_{sc} of the regular film has degraded to a higher rate than inverted structured PSC.[190] Though moving of electron contact to the rear side is a possible explanation, detailed reasoning requires further investigation. Incorporation of a [6,6]-phenyl-C_{61}-butyric acid methyl ester (PCBM) interlayer and high-quality perovskite absorber fabricated by thermal evaporation–spin coating method produces a hysteresis-free planar perovskites.[76]

Ions accumulate at the ion-blocking interface. The "p" and "n" doping induce ion migration at ion-blocking interface. These doping will screen the applied voltage and alter charge collection capability, resulting in hysteresis. In addition, ion migration is responsible for unusual
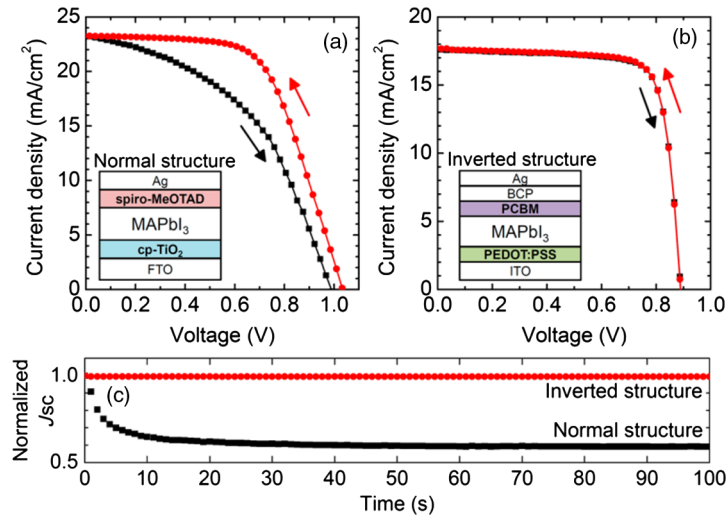
Fig. 18 I–V hysteresis and time-dependent photocurrent. (a) Scan direction-dependent I–V curves of the cp-TiO$_2$/MAPbI$_3$/spiro-MeOTAD (normal) structure and (b) the PEDOT:PSS/MAPbI$_3$/PCBM (inverted) structure. (c) Normalized time-dependent J_{sc} of normal and inverted structures. Open-circuit condition under one sun illumination was maintained before measuring J_{sc}. Reprinted with permission from Ref. 190. © 2015 by the American Chemical Society.

behaviors in perovskites materials such as photo-induced phase separation,[191] photoinduced giant dielectric constant,[192] and absence of transistor behavior at room temperature.[193] In high efficient PSC cells, ion migration does not cause hysteresis.[182] Ion migration within crystal structure,[194] which is also a major contributing factor for hysteresis, has a profound effect on device stability.[195] Experimental proof and test results show that ions migrate along the grain boundaries.[196]

4.4 *Moisture*

Moisture acts as a catalyst, and its presence tends to induce hydrolysis[107] in PSC, thereby converting PSC back to precursors, which is irreversible. Experiments to evaluate the stability of PSC against moisture were conducted in inert and other carrier gases to ascertain degradation exclusively due to moisture.[12] When exposed to moisture, perovskite structure tends to hydrolyze, undergoing irreversible degradation and decomposing back into precursors. Highly hygroscopic CH_3NH_3X converts to $CH(NH_2)_2X$ salts and PbX_2, with X = halide.[197] Heat, electric field, and ultraviolet exposure[198] accelerate this process. Figure 19 shows the mechanism of degradation:
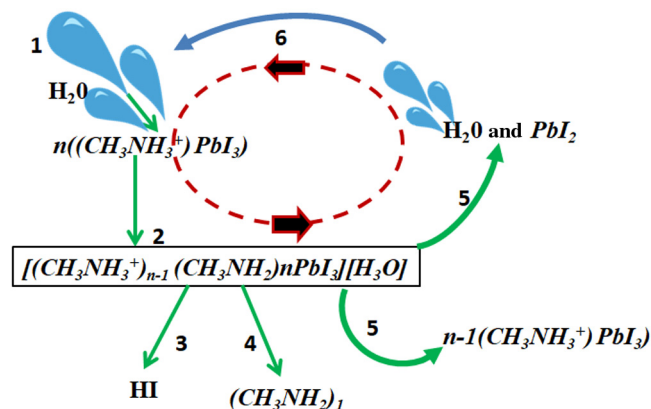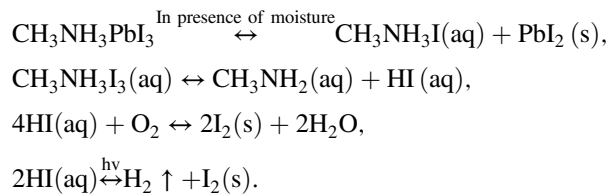

Fig. 19 Proposed decomposition pathway of $CH_3NH_3PbI_3$ in the presence of a water molecule.[197]

$$CH_3NH_3PbI_3 \overset{\text{In presence of moisture}}{\leftrightarrow} CH_3NH_3I(aq) + PbI_2(s),$$

$$CH_3NH_3I_3(aq) \leftrightarrow CH_3NH_2(aq) + HI(aq),$$

$$4HI(aq) + O_2 \leftrightarrow 2I_2(s) + 2H_2O,$$

$$2HI(aq) \overset{hv}{\leftrightarrow} H_2 \uparrow + I_2(s).$$

Stability of PSC, due to moisture, requires evaluation in three modes. One is purely because of moisture, the second is under the influence of moisture along with light, and finally the third mode is a combination of moisture along with light and oxygen. Degradation of perovskites is reported to follow the mechanism of Grotthuss.[199] In this, one water molecule reacts with perovskite material and degrades to HI and CH_3NH_2. Further, HI reacts with O_2 to form water, to initiate more deterioration. After exposing perovskite film $CH_3NH_3PbI_3$ to 80% RH for 2.5 h, the possibility of intermediate crystalline phase such as a hydrated compound $(CH_3NH_3)_4.PbI_6.H_2O$ exists. Grazing incidence x-ray diffraction (GIXRD) confirms the formation of intermediate phase. XRD pattern shows strong peaks of hydrate at 8.42 deg and 10.46 deg, which confirm the existence of intermediate phase. Exposure of solar cell to RH of 0% to 50% has led to very little degradation. However, under 90% RH, it showed a rapid decrease in PV performance efficiency from 12% to less than 1% in just 3 days. Third day values are $J_{sc} = 3.1 \text{ mA cm}^{-2}$, $V_{oc} = 0.637$, and FF = 0.36, $\eta = 0.7$.[200] Increase in RH level beyond 55% resulted in a drastic increase in degradation rate. In addition to general characterization, a powerful method such as photothermal deflection spectroscopy evaluates the changes in absorption after exposing perovskites to moisture.[201] In Fig. 20, $CH_3NH_3PbI_3$ shows absorption edge as ~1.57 eV, which shifts to 2.3 eV on exposure to moisture, this correspondence to PbI_2 formation, and decomposition of $CH_3NH_3PbI_3$. Figure 21 shows PCE versus heterojunction solar cells variation based on $MAPb(I_{1-x}Br_x)_3$ ($x = 0$, 0.06, 0.20, 0.29) as per time, stored without encapsulation at room temperature with RH ranging from 35% to 55%.[202] It also shows variation in UV–vis spectra as per moisture content and variation in the morphology. $CH_3NH_3PbBr_3$-based perovskites are less sensitive to moisture than PbI_X-based Perovskites. However, the absorption capacity of pure $CH_3NH_3PbI_3$ is not comparable to that of $CH_3NH_3PbBr_3$.[55,203] The first line of defense against the moisture is the top charge-transporting layer of the device. Resistance to moisture can be increased by inherently strengthening the bond between cation and metal halide.[200] Few other approaches are inclusion of thin blocking layer between perovskites and HTL, such as Al_2O_3,[169,204] moisture-blocking hole transporters,[205] and hydrophobic carbon electrodes.[2,116,206–209] Incorporation of 2-D PSC with large aromatic phenyl ethylammonium (PEA) cations could achieve average PCE of 5.5% with excellent stability against moisture. After exposure of these 2-D PSCs for more than 90 h at $72 \pm 2\%$ RH, they were stable and maintained 50% PCE of initial value.[210] Incorporating polyethylenimine
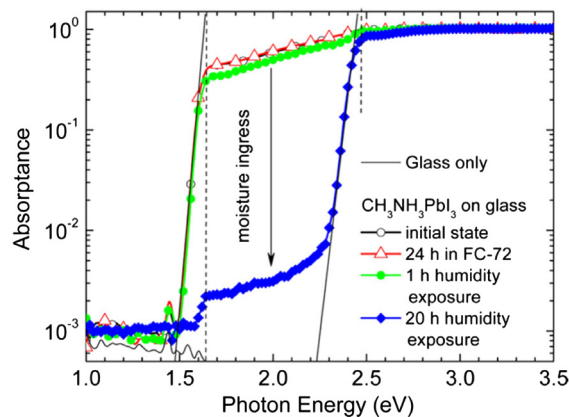

Fig. 20 PDS spectra of $CH_3NH_3PbI_3$ films before (initial state) and after exposure to a relative humidity of 30% to 40% for varied time period. Reprinted with permission from Ref. 201. © 2013 by the American Chemical Society
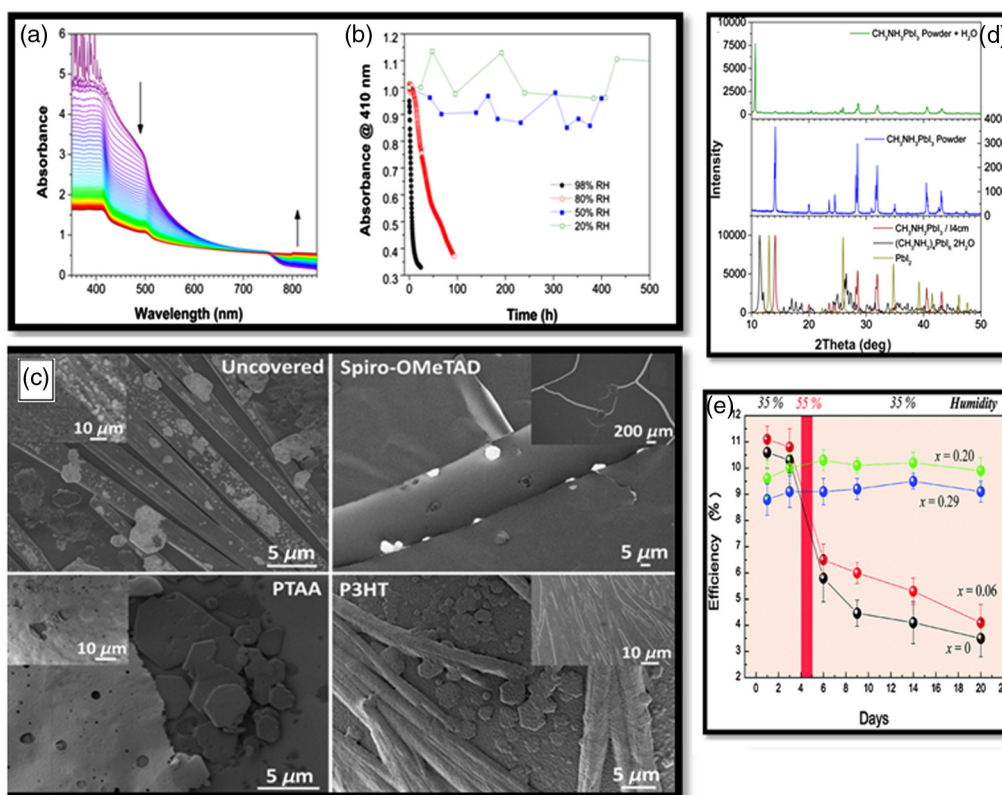
Fig. 21 Effect of moisture: (a) *in situ* absorbance measurements of $CH_3NH_3PbI_3$ exposed to 98% relative humidity. Measurements were taken at 15 min intervals, (b) normalized absorbance measurements (taken at 410 nm) for $CH_3NH_3PbI_3$ films exposed to different relative humidity, (c) SEM images of uncoated $CH_3NH_3PbI_3$, $CH_3NH_3PbI_3$/spiro-OMeTAD, $CH_3NH_3PbI_3$/PTAA, and $CH_3NH_3PbI_3$/P3HT films after exposure to 98% RH for 24 h. (d) Powder x-ray diffraction patterns for a sample of $CH_3NH_3PbI_3$ powder. Reprinted with permission from Ref. 202. © 2015 by the American Chemical Society. (e) PCE versus heterojunction variation on $MAPb(_{1-x}Br_x)3$ ($x = 0$, 0.06, 0.20, 0.29) with time stored in air at room temperature without encapsulation. Reprinted with permission from Ref. 61. © 2013 by the American Chemical Society.

cations in 2-D PSC helps in attaining better film quality and resistance to moisture degradation with PCE of 8.77%.[211] In addition, near-single-crystalline-type thin films are fabricated, which have, preferential out-of-plane alignment of crystallographic planes, good charge transport, and moisture resistance.[117] Thus, 2-D PSC has better moisture resistance capability than the 3-D PSC.[212,213]

Solution-processed $MAPbI_3$ was immune to changes when exposed to O_2. The decomposition on exposure to moisture or ambient air is due to H_2O.[202] However, very low quantity H_2O acts as an n-dopant for $MAPbI_3$, affecting the energy level. Proposed decomposition of $MAPbI_3$ eventually releases NH_3 and HI as volatile species, leaving PbI_2 and making decomposition reaction irreversible. Reports confirm that moisture coupled with light directly led to decomposition of $MAPbI_3$ to PbI_2, which was an irreversible reaction. Residuals such as PbI_2 and I_2 are formed easily under sunlight, instead of reversible hydrate in the dark, when $MAPbI_3$ exposed to an environment of 18 h at 60% RH.[107] Though the analysis of stability in dark is a basic test, stability research under illumination is essential for evaluation of working efficiency and degradation factor. Unlike degradation in the dark, exposure to moisture in light leads to irreversible decomposition of $MAPbI_3$ to PbI_2.

4.5 *Light Spectrum (UV and Visible)*

Mostly laboratory experiments are conducted under controlled light source such as LED. However, actual utilization involves sunlight with UV element, which accelerates degradation
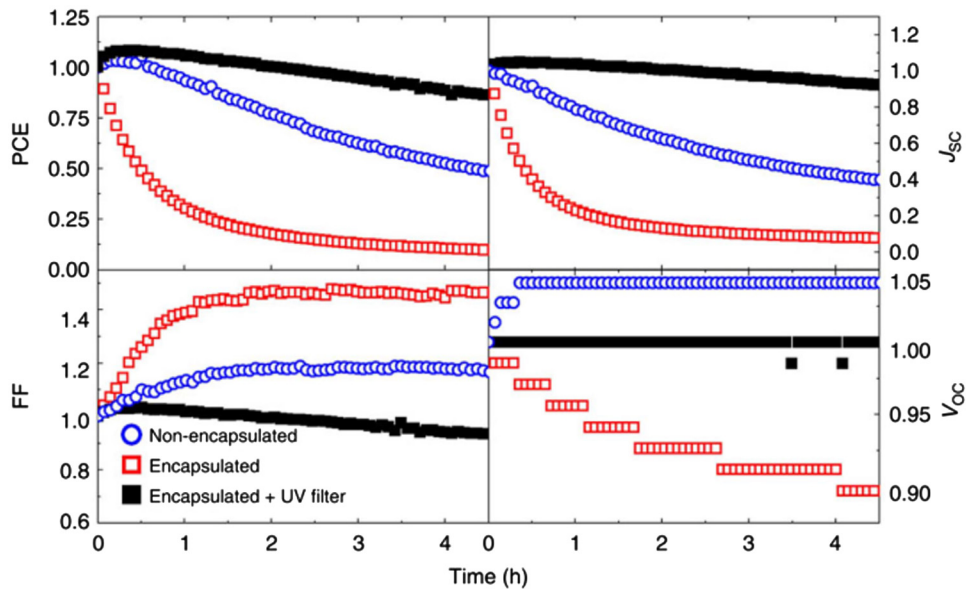
Fig. 22 Light soaking tests of regular PSCs under A.M. 1.5 G 1 Sun light intensity (with and without UV filters). Reproduced with permission from Ref. 148. © 2013 by Springer Nature.

pattern. The TiO_2 element in PSC, which is photocatalytic in the UV regime, assists degradation.[148] To further surprise, as shown in Fig. 22, degradation is higher in encapsulated devices than the unencapsulated devices for a conventional device.

This phenomenon is due to electrons injected into TiO_2 are entrapped in deep-lying unoccupied sites.[148] However, encapsulation along with UV-filter can enable attaining better results. Degradation is directly proportional to efficiency and follows a pattern of reduction in J_{sc}. A TiO_2-free mesoporous structured solar cell is comparatively less degradable than MSSC with TiO_2, which is confirmed by transient absorption spectroscopy. MSSC has a property of degradation being high at maximum power and rather low at open circuit condition. However, for practical applications installation of a UV filter on PSC overcomes the degradation process. Degradation is attributed to the instability problem[214] and the catalytic role of metal oxide when exposed to the UV spectrum. A general degradation mechanism for UV exposure is shown in Fig. 23. On exposure to UV light, photogenerated holes that are generated by absorption of energy react with the oxygen radicals adsorbed at surface oxygen vacancies. Molecular oxygen is absorbed from these sites, leading to a formation of unoccupied deep surface traps sites and a free electron per site. These electrons will recombine with the excess of holes in doped-hole transporter. On photoexcitation of sensitizer, electrons can follow in two ways. In the first route, they get injected into conduction band by which they get deeply trapped and in other they directly enter into the deep surface traps. These deeply trapped electrons are not mobile and recombine readily with holes on hole transporter.[148] The primary bottleneck that exists is transporting the charge. In quantum dots, polydispersity strongly affects transport. In quantum dot film, if few dots are of different sizes, then trap states manifest within the bandgap and lead to recombination. Similar is the case with 1-D carbon nanotubes. Three schemes are formulated to nullify the effects of UV. First being the reduction of trap sites or pacifying it and second is to undertake measures to avoid UV light reaching ETL (especially TiO_2). Finally, the third scheme is to replace TiO_2 scaffold with another material or make it TiO_2 free, which has been explored by Leijtens at el.[148] The efficiency of PSC device reduces to almost 0% after 12 h of exposure in a nonencapsulated format. However, with the introduction of Sb_2S_3 buffer layer in PSC, efficiency increased to ~65% of its initial value. This increase is due to the Sb_2S_3 blocking layer, which blocks the UV-induced photocatalysis in TiO_2, by providing a form of passivation. In addition, this extra layer assists in maintaining the crystalline structure of $CH_3NH_3PbI_3$.[215] A methodology such as usage of the downshifting molecule such as N-(2-(6-chloros-tetrazin-3-yloxy)ethyl)-naphthalimide (NITZ) with a strategy to suppress UV
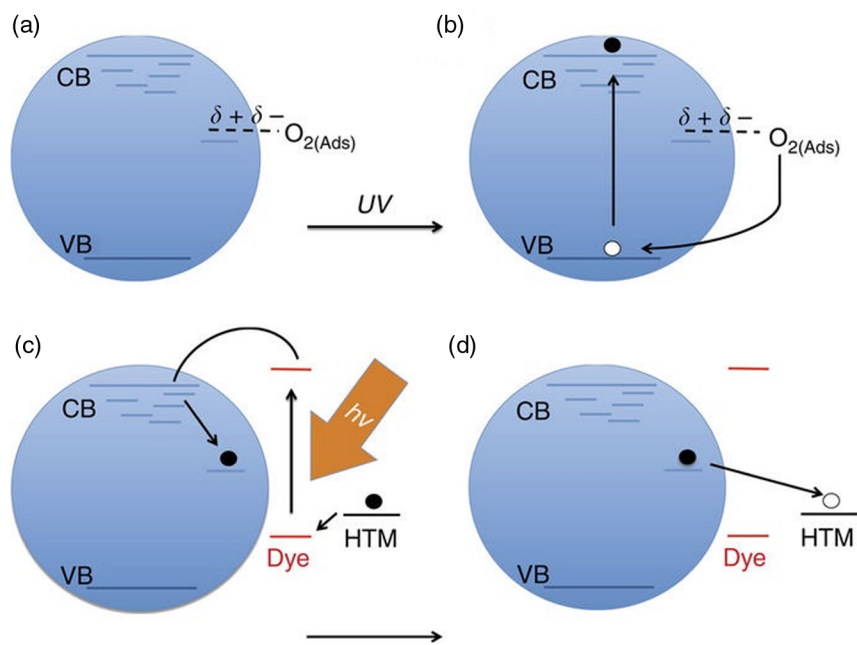
Fig. 23 Proposed mechanism for UV-induced degradation Reprinted with permission from Ref. 148. © 2013 by Springer Nature.

from the source is also explored, for UV protection in PSC.[216] They have a specialty to get excited in the UV spectrum and to emit into the visible spectrum, allowing UV photons utility.

4.6 *Thermal Stability*

Variation in efficiency and increase in temperature will result in amplification of deformities. These anomalies are due to deterioration in perovskites materials and behavior of HTM. It is understood that when the heat of the device ingresses into cell materials, mechanical stress of the materials at interfaces increases, thereby decreasing the lifetime of the PSC device. Accelerated aging test results showed that PbI_2 deteriorates much faster than $PbBr_2$, approximately after 60 min. High stability of Br is due to shorter and stronger bonds of Pb-Br compared to Pb-I.[217] Heating of $CH_3NH_3PbI_{3-x}Cl_x$ in N_2 environment at 90°C not only leads to the formation of 3-D perovskites structure but also results in a high rate of degradation at 100°C.[218] Hybrid perovskite assists in maintaining stability, as inorganic part of hybrid perovskites increases thermal stability and its organic part increases the stability of device. Comparison of formaldinium lead trihalide $(HC(NH_2)_2PbI_3)$ and $CH_3NH_3PbI_3$-based device reveals that the former is more stable as it deteriorates only after 290°C than the later, which decomposes at 230°C.[219] In PSC, deterioration rate due to temperature increases in the presence of moisture. Reports reveal that at 85°C time of decomposition is 283, 208, and 133 min when RH is 12%, 57%, and 85%, respectively.[220] Period of exposure is also an influential factor for evaluation and characterization by hard x-ray photoelectron spectroscopy instead of conventional XRD, because assessment is done on chemical content regardless of crystallinity of the sample. Mechanism of degradation is as follows:

$$CH_3NH_3PbI_3 \text{-} \rightarrow PbI_2 + CH_3NH_2 \uparrow + HI \uparrow .$$
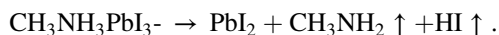
Films are made independent of parameters such as moisture and oxygen by subjecting it to ultrahigh vacuum heating chamber, to evaluate effects purely due to temperature.[221] I/Pb and N/Pb ratios define the characterization of films for degradation. Reduction of these ratios indicates degradation of perovskites into PbI_2, as shown in Fig. 24. Variation in temperature induces a different degree of degradation in various layers of PSC. For example, perovskites made of scaffolded ZnO are found to be more stable than TiO_2.[222,223]
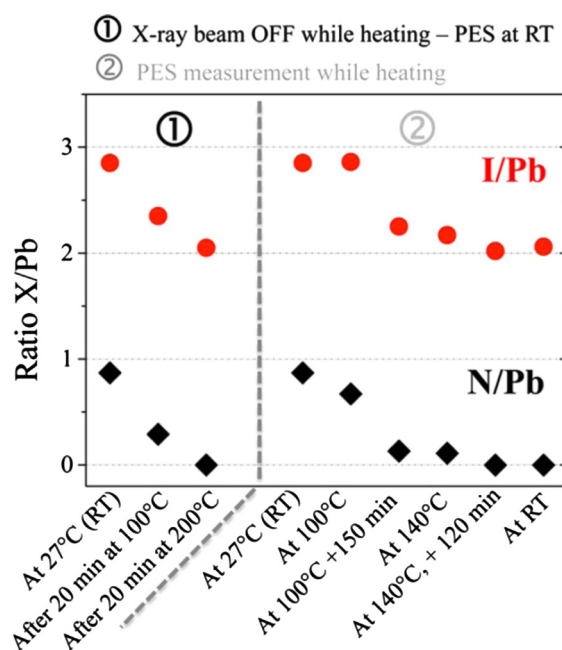
Fig. 24 I/Pb ratio (red circle) and N/Pb (black diamond) ratio plotted versus different temperatures. Reprinted with permission from Ref. 221. © 2015 by the American Chemical Society.

To understand degradation on perovskites purely due to thermal effects, semifabricated PSC, without HTL, ETL, and the top electrode are tested.[106] These semifinished planar structures undergo exposure to inert, O_2, and ambient conditions for 24 h. Surprisingly, degradation in the form of delamination happens in an ambient environment rather than in O_2. GIXRD and surface photovoltage measurements assisted in characterization and revealed that at temperature above 140°C and 160°C perovskite materials decomposed into PbI_2 in vacuum.[224] Up to 150°C, an increase in the Braggs peak with enhancement of perovskite film occurs. From 150°C to 200° C, these peaks reduced due to PbI_2 formation and further heating to 330°C lead to complete decomposition into Pb.[225] Empirical studies revealed that thermal annealing conducted for production of perovskite materials induces slight PbI_2 production, causing drop in efficiency. Heat treatment of layers such as ZnO before deposition lead to an increase in efficiency and thermal stability, due to reduction in deportation of methylammonium at the interface.[223] Thermal stability is a highly potent factor that affects different layers especially the HTM. Initiation of crystallization and formation of large crystals causing morphological hole traps affecting charge transportation and effecting PCE was reported for PSC with spiro-OMeTAD as HTM.[218] This crystalline process gets aggravated by additives or doping done in the layer to increase charge due to the hygroscopic nature of dopants.[226] To achieve better stability, many new HTM materials were explored, such as PTAA and 5,10,15-trihexyl-3,8,13-tris(4-methoxy-phenyl)-10,15-dihydro-5H-diindolo[3,2-a:3′,2′-c] carbazole (KR131).[227] Introduction of bulky aromatic PEA cations was reported to produce thermally stable 2-D PSC, which maintained 65% of its initial PSC after exposure to 100°C for 70 h.[210] In addition, multidimensional 3-D/2-D perovskites with an intermediate dimension between them led to the formation of thermally stable PSC, due to reduced defect density.[228]

4.7 Fabrication and Preparation

Fabrication is a vital factor for sustaining stability in PSC. It primarily constitutes two elements such as the synthesis method used and the substrate precursor. Synthesis temperature and time strongly influence the morphology, stability, and performance of PSC. In one-step deposition process, perovskite solution is dispensed on the substrate while turning at a fixed velocity. Though excess perovskite is spun off, perovskites crystallize on evaporation of the solvent.

Uncontrolled precipitation yields nonuniform large- and small-size crystals, resulting in poor performance and solar cell efficiency. Adhikari et al. have proposed the usage of an antisolvent method for better crystal formation and growth. It involves annealing conditions and defines charge transport capability, as measured by nanoscale Kelvin probe force microscopy (KPFM).[229] Annealing temperature effect on $CH_3NH_3PbI_3$ is analyzed from 80°C to 140°C as shown in Fig. 5. The peak of PbI_2 at 12.7°C, in XRD, increases proportionally as per the annealing temperature. The annealing time is optimized to achieve correct crystal size, charge transport layer such as HTL formed CZTS nanoparticles (CZTS-30).[230] Thermal annealing of $CH_3NH_3PbBr_3$ films at 90°C, for short duration such as ≤10 min, would lead to increased crystallinity, eliminating residual solvent and achieving complete conversion of the precursor to crystal, in comparison to longer annealing time.[231] Greater annealing time would initiate sublimation, so accurate monitoring of time is essential. For TiO_2 films, photonic curing technique is more effective than high-temperature annealing (∼500°C), as it creates more conductive films.[96] Photonic curing is also called pulse-thermal processing, which utilizes high-intensity plasma arc lamp. It delivers a peak sintering power up to 20,000 W/cm^2 for milliseconds and produces rapidly annealed thin films without damaging underlying plastic substrates. PEDOT:PSS-based PSC grown at room temperature without annealing was reported to exhibit a PCE of 14.27%.[232] They have high crystallinity when subjected to 40% RH at room temperature.[232]

4.8 Device Encapsulation

Air sensitivity of PSC elements, in conjunction with moisture sensitivity of perovskite absorbers, emphasizes the requirement of encapsulation of high level to attain a stable outdoor lifetime of over 25 years.[3,64,61] Without encapsulation, highly efficient devices were reported to degrade rapidly, showed 80% degradation when subjected to ambient temperature.[233] Usually, a thin glass coverslip is used to cover device, which is further sealed using a UV curable epoxy resin.[148,169,234] Ramos et al.[235] reported that single step high-temperature encapsulation (>150°C) resulted in delamination of active and metallization layers in devices. A two-step encapsulation approach minimizes the defect due to mechanical and thermal stress. The first step in a pre-encapsulation process consists of making electrical contact and later embedding it in a polymer matrix to ensure mechanical stability. The next step involves laminating the pre-encapsulated device using low temperature, to retain good photovoltaic characteristics of PSC. During the process and after, samples are monitored electrically (J–V curves). There are two types of configuration for encapsulation. Han et al. have compared these two types,[168] in first method, UV curable epoxy resin used to fill the area between silver contact and plain glass cover.[131,236–238] The other configuration has an electrode, which has a top glass cover with a gap in between. Water absorbent, desiccant material was made to fill this gap, thus absorbing moisture that had penetrated through epoxy resin sealant.[168] For 2-D PSC films, encapsulation becomes very critical. Therefore, plastic barrier films are used. It is available in two formats, namely partial and complete. They laminate commercial encapsulate adhesive on to films at 100°C. This type of encapsulation could only retard the ingress of moisture penetration and can maintain the operational performance of PSC steady for more than 1 year.[131,236,239–241] Conductive tapes made of commercial carbon assist in achieving a dual purpose such as terminal contact with perovskite and encapsulation. Encapsulated devices are leak tested with helium gas to assure moisture penetration. Investigations reveal that incorporation of impermeable barrier layers can be a long-term remedy to eliminate the ingress of moisture and oxygen.

5 Recombination

PSC (for $MAPbI_3$) has achieved laboratory PCE of 20.1% and an open-circuit voltage (V_{oc}) of 1.1 V, which is below theoretical V_{oc} limit of 1.32 V.[242] Loss of 200 mV is due to nonradiative recombination, which manifests itself at low external quantum yield (≲0.01%) for electroluminescence, corresponding to V_{oc}.[242,243] KPFM results of a single step and sequentially deposited films show that increase in potential barrier suppresses back recombination between electrons in TiO_2 and holes in perovskite.[244] A blocking layer is very crucial in a conventional PSC for

PbI_2 to inhibit charge-interception/recombination. Conversion of PbI_2 to $MAPbI_3$ occurs at solution interface of TiO_2/PbI_2 interface.[86]

6 Lead and Other Toxicity

Lead composition[245] leading to toxicity[108] and bioaccumulation in ecosystems[246] hamper the commercialization of organic-inorganic lead halide-based PSC. A PSC with $CH_3NH_3PbI_3$ as absorber material would contain about one-third lead by weight. On exposure to rainwater, perovskite will completely dissolve in water leaving behind PbI_2.[75]

Evaluations show that a PSC panel releases only 70 ppm of lead. This concentration is moderately low in comparison to the standards for low levels of contamination.[247] Though it is undesirable and not catastrophic, there is no accepted safe threshold for lead exposure.

In additional, other elements such as iodine[248,249] and methylamine[250] also have a high degree of toxicity. $MAPbI_3$ nanoparticles get airborne and affect the respiratory system, mix with fluids of the body, and reach brain and nerves.[251] Daniele et al. have reported the formation of PSC without lead using transition materials such as Cu. They developed $(CH_3NH_3)2CuCl_xBr_{4-x}$ series and confirmed green photoluminescence due to Cu+ ions formation. Mixing of halides $MA_2CuCl_xBr_{4-x}$ and chlorine with it will ensure appreciable stability, as it highly deliquescent.[252] Impedance spectroscopy was used to evaluate performance. Strong anisotropy and low absorption coefficient hamper these cells. The exact material combination decides the thickness of films and light harvesting requirement with limited diffusion length. Tin (Sn)[253–257] is also considered an apt replacement of Pb as it belongs to group 14 metal, with four electrons in its outer shell. However, due to the bigger size of metal in group 14, it induces instability of 2+ oxidation state.[139] Theoretical investigations reveal that I-5p orbitals of I_3^- groups influence band-edge reconstruction. This leads to new conduction–band minimum at Brillouim zone, which facilitated the formation of lead-free perovskites.[258] Lead-free perovskites films such as $CH_3NH_3SnX_3$ ($X = $ I, Br, Cl) is synthesized by vapor-assisted solution processing[253,259] and hot injection method.[255] Halide double perovskites utilize interplay between two metal ions to achieve this goal.[260,261] Replacing Pb^{2+} sites with a combination of trivalent Bi^{3+} and monovalent Ag^+ cations has led to the formation of 3-D double perovskites.[262,263]

7 Stability Comparison of 2-D and 3-D PSC

A comparative study shows 2-D PSC is more stable, up to 1400 h than 3-D PSC, when tested under the light source of AM 1.51 without any UV filters.[117] They retain about 80% of their original value, whereas 3-D PSC has a dramatic loss in efficiency. Thus, 2-D perovskites showed superior stability and water resistance.[117,264,265] Quasi-2-D (n-butylammonium)2(MA)2Pb3I10 has an efficiency of 12% with a drop in performance only after 2250 h.[117] Grancini and coworkers have integrated 2-D/3-D perovskite to combine advantages of both. Their interface has a combined benefit of excellent stability, excellent charge transport of 2-D perovskites, and absorption quality of 3-D perovskites.[266] The ability to collect ions to assemble into a stable 3-D perovskite structure is predicted by the Goldschmidt tolerance factor, "t." It is a stability indicator of a perovskite crystal, which describes the compatibility of ions with other materials in PSC. An ideal Goldschmidt tolerance factor should be below or equal to 1; for guanidinium, it is 1.03. For a perfect cubic perovskite structure $t = 1$. However, practically, one can expect ions to form a cubic 3-D structure if $0.9 \leq t \leq 1$. However, when $0.7 \leq t \leq 0.9$, it enables the formation of lower symmetry structures, such as tetragonal, rhombohedral, hexagonal, and orthorhombic.[267] Recent research at EPFL has reported enlarging the stability of methylammonium lead iodide perovskites, by introducing large organic cation. A promising member such as guanidinium (CH6N3+) is an example of a large organic cation group. It enhances the material's overall thermal and environmental stability for 3-D perovskites. Figure 25 shows the SEM image of 3-D PSC achieved efficiency over 19% ($19.2 \pm 0.4\%$) and sustaining its performance for 1000 h under continuous light illumination.[268] Chen et al.[269] have reported to achieve exceptional PCE for 2-D format using simple solution process and to achieve a vertical alignment of 2-D
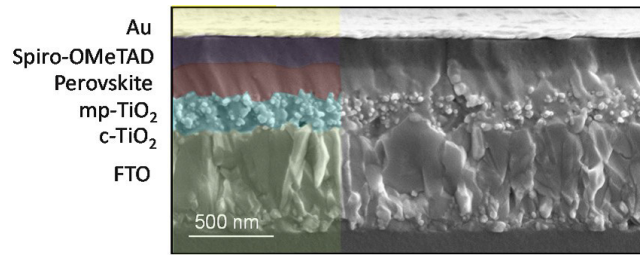
Fig. 25 Cross-sectional SEM image of a typical mixed MA:guanidinium PSC containing 14% of guanidinium. Device architecture: glass/FTO/c-TiO$_2$/ mp-TiO$_2$/perovskite/spiro-OMeTAD/Au. Reprinted with permission from Ref. 268. © 2017 by Springer Nature.
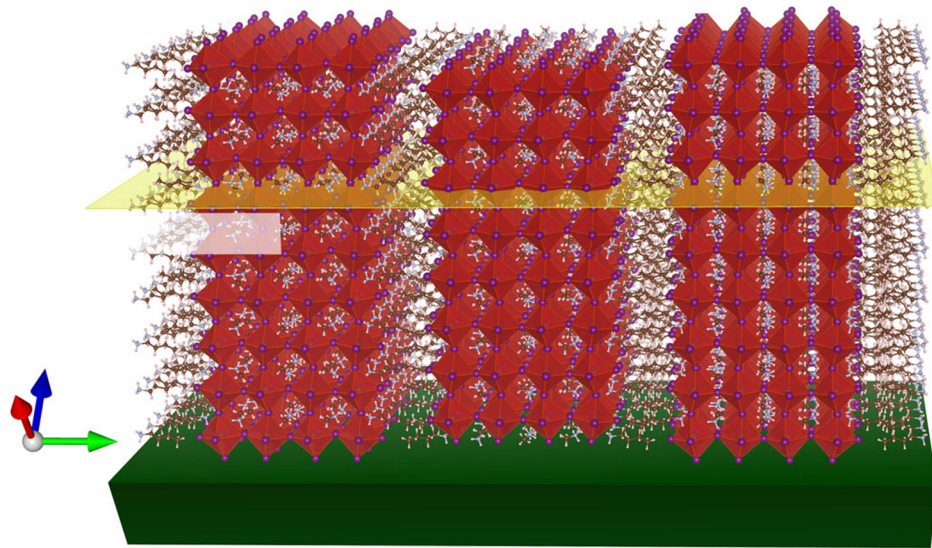

Fig. 26 Illustration of an orthorhombic (101) vertically oriented 2-D perovskite structure, with (202) planes parallel to substrate. Reprinted with permission from Ref. 269. © 2018 by Springer Nature.

perovskite layers to electrodes. Figure 26 shows the vertical orientation of (101) planes and (202) planes parallel to the substrate.[269]

8 Outlook

PSCs are an excellent and advantageous replacement for silicon solar cells. Positive features such as excellent absorption coefficient, ability to tune bandgap, ability to form flexible solar cells, compatibility with the solar spectrum, and good charge mobility make it a good performance solar cell. The hybrid feature of PSC, utilizing the advantages of organic and inorganic components in it, has enabled it to achieve efficiency at par with silicon solar cell and beyond. Perovskites absorber materials coupled with silicon solar cells, in a tandem cell format, could obtain a PCE above 30%. Replacing PSC with better HTM and innovative materials would enhance the PCE. Various combinations and materials are first tested in N$_2$ environment in the encapsulated form before further investigation and exploration. Major hindrances in its commercialization are its stability factor and toxicity. Our survey of the literature assures that continuous progress and development is going on to resolve these hindrances. In addition to the energy-related application, perovskites have an enhanced implication in numerous other domains such as flexible optoelectronics, supercapacitors, rechargeable batteries, and other hybrid systems that couple with photovoltaic cells. The futuristic application is to paste PSC films on buildings and skyscrapers enabling them to produce power and become self-sufficient. Testing methodology

process is also wholly restructured to reduce research time on combinations, which cannot be commercialized. Recently, a new fast and low threshold photography method has been developed by Aalto University in Finland to detect even a slight disintegration in a perovskite structure. This method provides more reliable results than optical measurement devices and is less complicated with fewer labor requirements than conventional x-ray crystallography. Encapsulation methodology is also revamped to handle moisture ingress issues. As this adds to the cost of manufacturing, researchers have recently reported the fabrication of air-stable PSC in 2-D format. To date, PSC has achieved a high PCE of 23.3%. Development of innovative materials for perovskites and their combination with PSC to tailor a new increased PCE along with applications in other domains is still yet to be unlocked.

Acknowledgments

References

1. A. Stoppato, "Life cycle assessment of photovoltaic electricity generation," *Energy* **33**(2), 224–232 (2008).
2. H. Zhou et al., "Low-temperature processed and carbon-based $ZnO/CH_3NH_3PbI_3/C$ planar heterojunction perovskite solar cells," *J. Phys. Chem. C* **119**(9), 4600–4605 (2015).
3. H. S. Kim et al., "Lead iodide perovskite sensitized all-solid-state submicron thin film mesoscopic solar cell with efficiency exceeding 9%," *Sci. Rep.* **2**, 591 (2012).
4. https://academic.microsoft.com (18 November).
5. National Renewable Energy Laboratory, "Efficiency chart," 2018, https://www.nrel.gov/pv/assets/pdfs/pv-efficiencies.
6. W. S. Yang et al., "Iodide management in formamidinium-lead-halide-based perovskite layers for efficient solar cells," *Science* **356**(6345), 1376–1379 (2017).
7. M. Saliba et al., "Cesium-containing triple cation perovskite solar cells: improved stability, reproducibility and high efficiency," *Energy Environ. Sci.* **9**(6), 1989–1997 (2016).
8. W. S. Yang et al., "High-performance photovoltaic perovskite layers fabricated through intramolecular exchange," *Science* **348**(6240), 1234–1237 (2015).
9. Q. Chen et al., "Interface engineering of highly efficient perovskite solar cells," *Science* **345**(6196), 542–546, (2014).
10. D. Liu and T. L. Kelly, "Perovskite solar cells with a planar heterojunction structure prepared using room-temperature solution processing techniques," *Nat. Photonics* **8**(2), 133–138 (2014).
11. J. T. W. Wang et al., "Low-temperature processed electron collection layers of graphene/TiO_2 nanocomposites in thin film perovskite solar cells," *Nano Lett.* **14**(2), 724–730 (2014).
12. J. Burschka et al., "Sequential deposition as a route to high-performance perovskite-sensitized solar cells," *Nature* **499**(7458), 316–319 (2013).
13. T. M. Akihiro Kojima et al., "Organometal halide perovskites as visible-light sensitizers for photovoltaic cells," *J. Am. Chem. Soc.* **131**(October), 6050–6051 (2009).
14. J.-H. Im et al., "6.5% efficient perovskite quantum-dot-sensitized solar cell," *Nanoscale* **3**(10), 4088–4093 (2011).
15. Q. Dong et al., "Electron-hole diffusion lengths >175 μm in solution-grown $CH_3NH_3PbI_3$ single," *Science* **347**(6225), 967–970 (2015).
16. W. Chen et al., "Efficient and stable large-area perovskite solar cells with inorganic charge extraction layers," *Science* **350**(6263), 944–948 (2015).
17. M. Liu et al., "Efficient planar heterojunction perovskite solar cells by vapor deposition," *Nature* **501**(7467), 395–398 (2013).

18. L. Yalçin and R. Öztürk, "Performance comparison of c-Si, mc-Si and a-Si thin film PV by PVsyst simulation," *J. Optoelectron. Adv. Mater.* **15**(3–4), 326–334 (2013).
19. C. D. Bailie et al., "Semi-transparent perovskite solar cells for tandems with silicon and CIGS," *Energy Environ. Sci.* **8**(3), 956–963 (2015).
20. W. Shockley and H. J. Queisser, "Detailed balance limit of efficiency of p-n junction solar cells," *J. Appl. Phys.* **32**(3), 510–519 (1961).
21. W.-J. Yin et al., "Halide perovskite materials for solar cells: a theoretical review," *J. Mater. Chem. A* **3**(17), 8926–8942 (2015).
22. J. A. Christians et al., "Tailored interfaces of unencapsulated perovkite solar cells for >1000 hour operational stability," *Nat. Energy* **3**(January), 68–74 (2018).
23. S. Chu, Y. Cui, and N. Liu, "The path towards sustainable energy," *Nat. Mater.* **16**(1), 16–22 (2017).
24. J. Zhang et al., "Life cycle assessment of titania perovskite solar cell technology for sustainable design and manufacturing," *ChemSusChem* **8**(22), 3882–3891 (2015).
25. S. Agarwal and P. R. Nair, "Device engineering of perovskite solar cells to achieve near ideal efficiency," *Appl. Phys. Lett.* **107**(12), 123901 (2015).
26. C. Wehrenfennig et al., "High charge carrier mobilities and lifetimes in organolead trihalide perovskites," *Adv. Mater.* **26**(10), 1584–1589 (2014).
27. K. Tvingstedt et al., "Radiative efficiency of lead iodide based perovskite solar cells," *Sci. Rep.* **4**, 1–7 (2014).
28. E. D. Kosten et al., "Highly efficient GaAs solar cells by limiting light emission angle," *Light Sci. Appl.* **2**, e45 (2013).
29. O. Höhn et al., "Maximal power output by solar cells with angular confinement," *Opt. Express* **22**, A715–A722 (2014).
30. J. L. Balenzategui et al., "Photon recycling and Shockley's diode equation," *J. Appl. Phys.* **4067**(8), 4067–4075 (1997).
31. O. D. Miller, E. Yablonovitch, and S. R. Kurtz, "Strong internal and external luminescence as solar cells approach the Shockley–Queisser limit," *IEEE J. Photovolatics* **2**(3), 303–311 (2012).
32. N. J. Jeon et al., "Compositional engineering of perovskite materials for high-performance solar cells," *Nature* **517**(7535), 476–480 (2015).
33. P. Jain et al., "Multiferroic behavior associated with an order–disorder hydrogen bonding transition in metal–organic frameworks (MOFs) with the perovskite ABX3 architecture," *J. Am. Chem. Soc.* **131**(38), 13625–13627 (2009).
34. L. C. Gómez-Aguirre et al., "Magnetic ordering-induced multiferroic behavior in $[CH_3NH_3][Co(HCOO)_3]$ metal–organic framework," *J. Am. Chem. Soc.* **138**(4), 1122–1125 (2016).
35. R. Comin et al., "Low trap-state density and long carrier diffusion in organolead trihalide perovskite single crystals," *Science* **347**(6221), 519–522 (2015).
36. S. D. Stranks et al., "Electron-hole diffusion lengths exceeding 1 micrometer in an organo-metal trihalide perovskite absorber," *Science* **342**(6156), 341–344 (2013).
37. S. Sien et al., "Long range balanced electron and hole transport lengths in organic inorganic $CH_3NH_3PbI_3$," *Science* **342**, 344–347 (2013).
38. T. M. Brenner et al., "Hybrid organic–inorganic perovskites: low-cost semiconductors with intriguing charge-transport properties," *Nat. Rev. Mater.* **1**(1), 15007 (2016).
39. M. B. Johnston and L. M. Herz, "Hybrid perovskites for photovoltaics: charge-carrier recombination, diffusion, and radiative efficiencies," *Acc. Chem. Res.* **49**(1), 146–154 (2016).
40. L. C. Schmidt et al., "Nontemplate synthesis of $CH_3NH_3PbBr_3$ perovskite nanoparticles," *J. Am. Chem. Soc.* **136**(3), 850–853 (2014).
41. F. Deschler et al., "High photoluminescence efficiency and optically pumped lasing in solution-processed mixed halide perovskite semiconductors," *J. Phys. Chem. Lett.* **5**(8), 1421–1426 (2014).
42. B. O'Regan and M. Grätzel, "A low-cost, high-efficiency solar cell based on dye-sensitized colloidal TiO_2 films," *Nature* **353**, 737–740 (1991).

43. Q. Zhang et al., "Small-molecule solar cells with efficiency over 9%," *Nat. Photonics* **9**, 35–41 (2015).

44. A. Abate et al., "Efficient luminescent solar cells based on tailored mixed-cation perovskites efficient luminescent solar cells based on tailored mixed-cation perovskites," *Appl. Opt.* **2**(1), e1501170 (2016).

45. Z.-K. Tan et al., "Bright light-emitting diodes based on organometal halide perovskite," *Nat. Nanotechnol.* **9**(9), 687–692 (2014).

46. J. Wang et al., "Interfacial control toward efficient and low-voltage perovskite light-emitting diodes," *Adv. Mater.* **27**(14), 2311–2316 (2015).

47. Q. Lin et al., "Low noise, IR-blind organohalide perovskite photodiodes for visible light detection and imaging," *Adv. Mater.* **27**(12), 2060–2064 (2015).

48. R. Dong et al., "High-gain and low-driving-voltage photodetectors based on organolead triiodide perovskites," *Adv. Mater.* **27**(11), 1912–1918 (2015).

49. X. Hu et al., "High-performance flexible broadband photodetector based on organolead halide perovskite," *Adv. Funct. Mater.* **24**(46), 7373–7380 (2014).

50. H. Zhu et al., "Lead halide perovskite nanowire lasers with low lasing thresholds and high quality factors," *Nat. Mater.* **14**(6), 636–642 (2015).

51. L. Wang et al., "Device performance of the mott insulator $LaVO_3$ as a photovoltaic material," *Phys. Rev. Appl.* **3**(6), 064015 (2015).

52. E. Assmann et al., "Oxide heterostructures for efficient solar cells," *Phys. Rev. Lett.* **110**(7), 078701 (2013).

53. J. Zhang et al., "N-Type doping and energy states tuning in $CH_3NH_3Pb_{1-x}Sb_{2x/3}I_3$ perovskite solar cells," *ACS Energy Lett.* **1**(3), 535–541 (2016).

54. C. Roldan-Carmona et al., "High efficiency single-junction semitransparent perovskite solar cells," *Energy Environ. Sci.* **7**(9), 2968–2973 (2014).

55. Z. Cheng and J. Lin, "Layered organic-inorganic hybrid perovskites: structure, optical properties, film preparation, patterning and templating engineering," *CrystEngComm* **12**(10), 2646–2662 (2010).

56. Q. Chen et al., "Under the spotlight: the organic–inorganic hybrid halide perovskite for optoelectronic applications," *Nano Today* **10**(3), 355–396 (2015).

57. L. Dou et al., "Atomically thin two-dimensional organic-inorganic hybrid perovskites," *Science* **349**(6255), 1518–1521 (2015).

58. P. Tyagi, S. M. Arveson, and W. A. Tisdale, "Colloidal organohalide perovskite nanoplatelets exhibiting quantum confinement," *J. Phys. Chem. Lett.* **6**(10), 1911–1916 (2015).

59. D. Zhang et al., "Ultrathin colloidal cesium lead halide perovskite nanowires," *J. Am. Chem. Soc.* **138**(40), 13155–13158 (2016).

60. L. C. Chen et al., "Annealing effects on high-performance $CH_3NH_3PbI_3$ perovskite solar cells prepared by solution-process," *Sol. Energy* **122**, 1047–1051 (2015).

61. J. H. Noh et al., "Chemical management for colorful, efficient, and stable inorganic–organic hybrid nanostructured solar cells," *Nano Lett.* **13**, 1764–1769 (2013).

62. A. H. Slavney et al., "A bismuth-halide double perovskite with long carrier recombination lifetime for photovoltaic applications," *J. Am. Chem. Soc.* **138**(7), 2138–2141 (2016).

63. L. Etgar et al., "Mesoscopic $CH_3NH_3PbI_3/TiO_2$ heterojunction solar cells," *J. Am. Chem. Soc.* **134**(42), 17396–17399 (2012).

64. M. M. Lee et al., "Efficient hybrid solar cells based on meso-superstructured organometal halide perovskites," *Science* **338**(6107), 643–647 (2012).

65. A. Yella et al., "Porphyrin-sensitized solar cells with cobalt (II/III)-based redox electrolyte exceed 12 percent efficiency," *Science* **334**(6056), 629–634 (2011).

66. S. K. Pathak et al., "Performance and stability enhancement of dye-sensitized and perovskite solar cells by Al doping of TiO_2," *Adv. Funct. Mater.* **24**(38), 6046–6055 (2014).

67. T. Gatti et al., "The renaissance of fullerenes with perovskite solar cells," *Nano Energy* **41**, 84–100 (2017).

68. P. Docampo et al., "Efficient organometal trihalide perovskite planar-heterojunction solar cells on flexible polymer substrates," *Nat. Commun.* **4**(27), 2761 (2013).

69. L. Yang, J. Wang, and W. W. F. Leung, "Lead iodide thin film crystallization control for high-performance and stable solution-processed perovskite solar cells," *ACS Appl. Mater. Interfaces* **7**(27), 14614–14619 (2015).

70. J. Song et al., "Low-temperature SnO$_2$-based electron selective contact for efficient and stable perovskite solar cells," *J. Mater. Chem. A* **3**(20), 10837–10844 (2015).

71. S. Aharon et al., "Depletion region effect of highly efficient hole conductor free CH$_3$NH$_3$PbI$_3$ perovskite solar cells," *Phys. Chem. Chem. Phys.* **16**(22), 10512–10518 (2014).

72. J. Shi et al., "Hole-conductor-free perovskite organic lead iodide heterojunction thin-film solar cells: high efficiency and junction property," *Appl. Phys. Lett.* **104**(6), 063901 (2014).

73. W. Schottky, "Vereinfachte und erweiterte Theorie der Randschicht-gleichrichter," *Zeitschrift f Phys.* **118**(9–10), 539–592 (1942).

74. Y. Jiang et al., "Optical analysis of perovskite/silicon tandem solar cells," *J. Mater. Chem. C* **4**(24), 5679–5689 (2016).

75. R. Asadpour et al., "Bifacial Si heterojunction-perovskite organic-inorganic tandem to produce highly efficient (η 33%) solar cell," *Appl. Phys. Lett.* **106**(24), 243902 (2015).

76. F. Fu et al., "Low-temperature-processed efficient semi-transparent planar perovskite solar cells for bifacial and tandem applications," *Nat. Commun.* **6**, 8932 (2015).

77. T. Todorov et al., "Perovskite-kesterite monolithic tandem solar cells with high open-circuit voltage," *Appl. Phys. Lett.* **105**(17), 173902 (2014).

78. C. W. Chu et al., "Integration of organic light-emitting diode and organic transistor via a tandem structure," *Appl. Phys. Lett.* **86**(25), 253503 (2005).

79. Z. Liu et al., "The application of highly doped single-layer graphene as the top electrodes of semitransparent organic solar cells," *ACS Nano* **6**(1), 810–818 (2011).

80. Y. H. Kim et al., "Combined alternative electrodes for semi-transparent and ITO-free small molecule organic solar cells," *Org. Electron. Phys. Mater. Appl.* **13**(11), 2422–2428 (2012).

81. A. Dubey et al., "A strategic review on processing routes towards highly efficient perovskite solar cells," *J. Mater. Chem. A* **6**(6), 2406–2431 (2018).

82. J. H. Im, H. S. Kim, and N. G. Park, "Morphology-photovoltaic property correlation in perovskite solar cells: one-step versus two-step deposition of CH$_3$NH$_3$PbI$_3$," *APL Mater.* **2**(8), 081510 (2014).

83. J. H. Heo, D. H. Song, and S. H. Im, "Planar CH$_3$NH$_3$PbBr$_3$ hybrid solar cells with 10.4% power conversion efficiency, fabricated by controlled crystallization in the spin-coating process," *Adv. Mater.* **26**(48), 8179–8183 (2014).

84. P. W. Liang et al., "Additive enhanced crystallization of solution-processed perovskite for highly efficient planar-heterojunction solar cells," *Adv. Mater.* **26**(22), 3748–3754 (2014).

85. D. T. Moore et al., "Crystallization kinetics of organic-inorganic trihalide perovskites and the role of the lead anion in crystal growth," *J. Am. Chem. Soc.* **137**(6), 2350–2358 (2015).

86. D. H. Cao et al., "Remnant PbI$_2$, an unforeseen necessity in high-efficiency hybrid perovskite-based solar cells?" *APL Mater.* **2**(9), 091101 (2014).

87. Q. Chen et al., "Planar heterojunction perovskite solar cells via vapor-assisted solution process," *J. Am. Chem. Soc.* **136**(2), 622–625 (2013).

88. C. J. Brabec and J. R. Durrant, "Solution-processed organic solar cells," *MRS Bull.* **33**(7), 670–675 (2008).

89. M. Graetzel et al., "Materials interface engineering for solution-processed photovoltaics," *Nature* **488**(7411), 304–312 (2012).

90. H. C. Liao et al., "Enhanced efficiency of hot-cast large-area planar perovskite solar cells/modules having controlled chloride incorporation," *Adv. Energy Mater.* **7**(8), 1601660 (2017).

91. W. Nie et al., "High-efficiency solution-processed perovskite solar cells with millimeter-scale grains," *Sol. Cells* **347**(6221), 522–526 (2015).

92. K. Hwang et al., "Toward large scale roll-to-roll production of fully printed perovskite solar cells," *Adv. Mater.* **27**(7), 1241–1247 (2015).

93. D. Vak et al., "3D printer based slot-die coater as a lab-to-fab translation tool for solution-processed solar cells," *Adv. Energy Mater.* **5**(4), 1401539 (2015).

94. R. R. Søndergaard, M. Hösel, and F. C. Krebs, "Roll-to-roll fabrication of large area functional organic materials," *J. Polym. Sci. Part B Polym. Phys.* **51**(1), 16–34 (2013).

95. A. T. Barrows et al., "Efficient planar heterojunction mixed-halide perovskite solar cells deposited via spray-deposition," *Energy Environ. Sci.* **7**(9), 2944–2950 (2014).

96. S. Das et al., "High-performance flexible perovskite solar cells by using a combination of ultrasonic spray-coating and low thermal budget photonic curing," *ACS Photonics* **2**(6), 680–686 (2015).

97. Z. Wang et al., "Stability of perovskite solar cells: a prospective on the substitution of the a cation and x anion," *Angew. Chemie—Int. Ed.* **56**(5), 1190–1212 (2017).

98. Z. Wei et al., "Inkjet printing and instant chemical transformation of a $CH_3NH_3PbI_3$/nanocarbon electrode and interface for planar perovskite solar cells," *Angew. Chem. Int. Ed.* **53**(48), 13239–13243 (2014).

99. J. H. Kim et al., "Enhanced environmental stability of planar heterojunction perovskite solar cells based on blade-coating," *Adv. Energy Mater.* **5**(4), 1401229 (2015).

100. H. C. Yeh et al., "All-small-molecule efficient white organic light-emitting diodes by multi-layer blade coating," *Org. Electron. Phys. Mater. Appl.* **13**(5), 914–918 (2012).

101. C. Y. Chen et al., "Continuous blade coating for multi-layer large-area organic light-emitting diode and solar cell," *J. Appl. Phys.* **110**(9), 094501 (2011).

102. T. M. Schmidt et al., "Upscaling of perovskite solar cells: fully ambient roll processing of flexible perovskite solar cells with printed back electrodes," *Adv. Energy Mater.* **5**(15), 1500569 (2015).

103. Z. Gu et al., "Interfacial engineering of self-assembled monolayer modified semi-roll-to-roll planar heterojunction perovskite solar cells on flexible substrates," *J. Mater. Chem. A* **3**(48), 24254–24260, (2015).

104. S. Kumar and A. Dhar, "Accelerated thermal-aging-induced degradation of organometal triiodide perovskite on ZnO nanostructures and its effect on hybrid photovoltaic devices," *ACS Appl. Mater. Interfaces* **8**(28), 18309–18320 (2016).

105. O. Haillant, "Accelerated weathering testing principles to estimate the service life of organic PV modules," *Sol. Energy Mater. Sol. Cells* **95**(5), 1284–1292 (2011).

106. B. Conings et al., "Intrinsic thermal instability of methylammonium lead trihalide perovskite," *Adv. Energy Mater.* **5**(15), 1500477 (2015).

107. A. M. A. Leguy et al., "Reversible hydration of $CH_3NH_3PbI_3$ in films, single crystals, and solar cells," *Chem. Mater.* **27**(9), 3397–3407 (2015).

108. R. A. Goyer, "Lead toxicity: current concerns," *Environ. Health Perspect.* **100**, 177–187 (1993).

109. Z. Yang et al., "Stabilized wide bandgap perovskite solar cells by tin substitution," *Nano Lett.* **16**(12), 7739–7747 (2016).

110. W. Qui et al., "Pinhole-free perovskite films for efficient solar modules," *Energy Environ. Sci.* **9**, 484–489 (2016).

111. M. Saliba et al., "Incorporation of rubidium cations into perovskite solar cells improves photovoltaic performance Incorporation of rubidium cations into perovskite solar cells improves photovoltaic performance," *Science* **354**(6309), 206–209 (2016).

112. L. Chu et al., "Boosting efficiency of hole conductor-free perovskite solar cells by incorporating p-type NiO nanoparticles into carbon electrodes," *Sol. Energy Mater. Sol. Cells* **178**, 164–169 (2018).

113. X. Lv et al., "Acylhydrazone-based porphyrin derivative as hole transport material for efficient and thermally stable perovskite solar cells," *Dye. Pigments* **160**, 957–961 (2019).

114. J. Cao et al., "Efficient, hysteresis-free, and stable perovskite solar cells with ZnO as electron-transport layer: effect of surface passivation," *Adv. Mater.* **30**(11), 1705596 (2018).

115. S. Seo et al., "Perovskite solar cells with inorganic electron- and hole-transport layers exhibiting long-term ($\approx$500 h) stability at 85°C under continuous 1 sun illumination in ambient air," *Adv. Mater.* **30**(29), 1801010 (2018).

116. A. Mei et al., "A hole-conductor-free, fully printable mesoscopic perovskite solar cell with high stability," *Science* **345**(6194), 295LP–298 (2014).

117. H. Tsai et al., "High-efficiency two-dimensional Ruddlesden–Popper perovskite solar cells," *Nature* **536**(7616), 312–316 (2016).

118. N. J. Jeon et al., "A fluorene-terminated hole-transporting material for highly efficient and stable perovskite solar cells," *Nat. Energy* **3**(8), 682–689 (2018).

119. N. Rolston et al., "Engineering stress in perovskite solar cells to improve stability," *Adv. Energy Mater.* **8**(29), 1802139 (2018).

120. H. Il Kim et al., "Improving the performance and stability of inverted planar flexible perovskite solar cells employing a novel NDI-based polymer as the electron transport layer," *Adv. Energy Mater.* **8**(16), 1702872 (2018).

121. C. Tian et al., "Fullerene derivative with a branched alkyl chain exhibits enhanced charge extraction and stability in inverted planar perovskite solar cells," *New J. Chem.* **42**(4), 2896–2902 (2018).

122. R. Chen et al., "Efficient and stable inverted planar perovskite solar cells using a triphenylamine hole-transporting material," *ChemSusChem* **11**(9), 1467–1473 (2018).

123. Y. Zhao et al., "Perovskite seeding growth of formamidinium-lead-iodide-based perovskites for efficient and stable solar cells," *Nat. Commun.* **9**(1), 1607 (2018).

124. T. Leijtens et al., "Tin-lead halide perovskites with improved thermal and air stability for efficient all-perovskite tandem solar cells," *Sustain. Energy Fuels* **2**, 2450–2459 (2018).

125. K. T. Cho et al., "Selective growth of layered perovskites for stable and efficient photovoltaics," *Energy Environ. Sci.* **11**(4), 952–959 (2018).

126. H. Zhang et al., "Improving the stability and performance of perovskite solar cells via off-the-shelf post-device ligand treatment," *Energy Environ. Sci.* **11**(8), 2253–2262 (2018).

127. T. Ye et al., "Efficient and ambient-air-stable solar cell with highly oriented 2D@3D perovskites," *Adv. Funct. Mater.* **28**(30), 1801654 (2018).

128. M. Najafi et al., "Highly efficient and stable flexible perovskite solar cells with metal oxides nanoparticle charge extraction layers," *Small* **14**(12), 1702775 (2018).

129. W. Li et al., "In situ induced core/shell stabilized hybrid perovskites via gallium(iii) acetylacetonate intermediate towards highly efficient and stable solar cells," *Energy Environ. Sci.* **11**(2), 286–293 (2018).

130. A. Baumann et al., "Persistent photovoltage in methylammonium lead iodide perovskite solar cells," *APL Mater.* **2**(8), 081501 (2014).

131. M. Jørgensen et al., "Stability of polymer solar cells," *Adv. Mater.* **24**(5), 580–612 (2012).

132. R. Peleg, "Aalto team finds significant shortcomings in aging tests performed on perovskite-based solar cells," 2018, https://www.perovskite-info.com/aalto-team-finds-significant-shortcomings-aging-tests-performed-perovskite-based-solar-cells (accessed 20 November 2019).

133. D. Bi et al., "Polymer-templated nucleation and crystal growth of perovskite films for solar cells with efficiency greater than 21%," *Nat. Energy* **1**(10), 16142 (2016).

134. A. Dualeh et al., "Thermal behavior of methylammonium lead-trihalide perovskite photovoltaic light harvesters," *Chem. Mater.* **26**(21), 6160–6164 (2014).

135. Y. Mashiyama et al., "Displacive character of the cubic-tetragonal transition in $CH_3NH_3PbX_3$," *J. Korean Phys. Soc.* **42**, S1026–S1029 (2003).

136. N. Onoda-Yamamuro, T. Matsuo, and H. Suga, "Calorimetric and IR spectroscopic studies of phase transitions in methylammonium trihalogenoplumbates (II)," *J. Phys. Chem. Solids* **51**(12), 1383–1395 (1990).

137. R. Venugopal, P. I. Lin, and Y. T. Chen, "Photoluminescence and Raman scattering from catalytically grown $Zn_xCd_{1-x}Se$ alloy nanowires," *J. Phys. Chem. B* **110**(24), 11691–11696 (2006).

138. R. Hill, "Energy-gap variations in semiconductor alloys," *J. Phys. C Solid State Phys.* **7**(3), 521–526 (1974).

139. F. Hao et al., "Lead-free solid-state organic-inorganic halide perovskite solar cells," *Nat. Photonics* **8**(6), 489–494 (2014).

140. J. Schoonman, "Organic-inorganic lead halide perovskite solar cell materials: a possible stability problem," *Chem. Phys. Lett.* **619**, 193–195 (2015).

141. Z. K. Wang et al., "Improved hole interfacial layer for planar perovskite solar cells with efficiency exceeding 15%," *ACS Appl. Mater. Interfaces* **7**(18), 9645–9651 (2015).

142. Y. Ogomi et al., "$CH_3NH_3Sn_xPb_{(1-x)}I_3$ perovskite solar cells covering up to 1060 nm," *J. Phys. Chem. Lett.* **5**(6), 1004–1011 (2014).

143. J. Berry et al., "Hybrid organic-inorganic perovskites (HOIPs): opportunities and challenges," *Adv. Mater.* **27**(35), 5102–5112 (2015).
144. M. A. Green, A. Ho-Baillie, and H. J. Snaith, "The emergence of perovskite solar cells," *Nat. Photonics* **8**(7), 506–514 (2014).
145. D. B. Mitzi et al., "Conducting layered organic-inorganic halides containing ⟨110⟩ oriented perovskite sheets," *Science* **267**(5203), 1473–1476 (1995).
146. V. D'Innocenzo et al., "Tuning the light emission properties by band gap engineering in hybrid lead-halide perovskite," *J. Am. Chem. Soc.* **136**(51), 17730–17733 (2014).
147. N. Adhikari et al., "Crystallization of a perovskite film for higher performance solar cells by controlling water concentration in methyl ammonium iodide precursor solution," *Nanoscale* **8**(5), 2693–2703 (2016).
148. T. Leijtens et al., "Overcoming ultraviolet light instability of sensitized TiO_2 with meso-superstructured organometal tri-halide perovskite solar cells," *Nat. Commun.* **4**, 2885 (2013).
149. J. C. Yu et al., "High-performance planar perovskite optoelectronic devices: a morphological and interfacial control by polar solvent treatment," *Adv. Mater.* **27**(23), 3492–3500 (2015).
150. H. Choi et al., "Combination of titanium oxide and a conjugated polyelectrolyte for high-performance inverted-type organic optoelectronic devices," *Adv. Mater.* **23**(24), 2759–2763 (2011).
151. B. R. Lee et al., "Surface modification of metal oxide using ionic liquid molecules in hybrid organic-inorganic optoelectronic devices," *J. Mater. Chem.* **21**(7), 2051–2053 (2011).
152. S. K. Hau et al., "Interfacial modification to improve inverted polymer solar cells," *J. Mater. Chem.* **18**(42), 5113–5119 (2008).
153. H. Ma et al., "Interface engineering for organic electronics," *Adv. Funct. Mater.* **20**(9), 1371–1388 (2010).
154. H. Zhou et al., "High-efficiency polymer solar cells enhanced by solvent treatment," *Adv. Mater.* **25**(11), 1646–1652 (2013).
155. B. R. Lee et al., "Amine-based polar solvent treatment for highly efficient inverted polymer solar cells," *Adv. Mater.* **26**(3), 494–500 (2014).
156. J. You et al., "Low-temperature solution-processed perovskite solar cells with high efficiency and flexibility," *ACS Nano* **8**(2), 1674–1680 (2014).
157. J. Jeng et al., "Nickel oxide electrode interlayer in $CH_3NH_3PbI_3$ perovskite/PCBM planar-heterojunction hybrid solar cells communication," *Adv. Mater.* **26**(24), 4107–4113 (2014).
158. A. Sarkar et al., "Three-dimensional nanoarchitecture of $BiFeO_3$ anchored TiO_2 nanotube arrays for electrochemical energy storage and solar energy conversion," *ACS Sustain. Chem. Eng.* **3**(9), 2254–2263 (2015).
159. Q. Wu et al., "Acetate salts as nonhalogen additives to improve perovskite film morphology for high-efficiency solar cells," *ACS Appl. Mater. Interfaces* **8**(24), 15333–15340 (2016).
160. K. Wojciechowski et al., "C 60 as an E ffi cient n-type compact layer in perovskite solar cells," *J. Phys. Chem. Lett.* **6**, 2399–2405 (2015).
161. J. Liu et al., "Copper thiocyanate : an efficient and affordable hole transporting material, toward thermally stable perovskite solar cells," *Adv. Mater. Interfaces(I)* **3**(22), 1600571 (2016).
162. J. Burschka et al., "Tris(2-(1H-pyrazol-1-yl)pyridine)cobalt(III) as p-type dopant for organic semiconductors and its application in highly efficient solid-state dye-sensitized solar cells," *J. Am. Chem. Soc.* **133**(45), 18042–18045 (2011).
163. J. Liu et al., "A dopant-free hole-transporting material for efficient and stable perovskite solar cells," *Energy Environ. Sci.* **7**(9), 2963–2967 (2014).
164. National Renewable Energy Laboratory, "Remarkable stability in perovskite solar cells," Science daily, 2, https://www.sciencedaily.com/releases/2018/02/180206115145.htm (accessed 16 August 2018).
165. H. Choi et al., "Facile scalable synthesis of MoO_2 nanoparticles by new solvothermal cracking process and their application to hole transporting layer for $CH_3NH_3PbI_3$ planar perovskite solar cells," *Chem. Eng. J.* **310**, 179–186 (2017).

166. S. Seo et al., "An ultra-thin, un-doped NiO hole transporting layer of highly efficient (16.4%) organic–inorganic hybrid perovskite solar cells," *Nanoscale* **8**(22), 11403–11412 (2016).

167. J. Y. Wang et al., "Bifunctional polymer nanocomposites as hole-transport layers for efficient light harvesting: application to perovskite solar cells," *ACS Appl. Mater. Interfaces* **7**(50), 27676–27684 (2015).

168. Y. Han et al., "Degradation observations of encapsulated planar $CH_3 NH_3 PbI_3$ perovskite solar cells at high temperatures and humidity," *J. Mater. Chem. A* **3**(15), 8139–8147 (2015).

169. S. Guarnera et al., "Improving the long-term stability of perovskite solar cells with a porous Al_2O_3 buffer layer," *J. Phys. Chem. Lett.* **6**(3), 432–437 (2015).

170. J. Wang et al., "Performance enhancement of perovskite solar cells with Mg-doped TiO_2 compact film as the hole-blocking layer," *Appl. Phys. Lett.* **106**(12), 121104 (2015).

171. W. Ke et al., "Efficient hole-blocking layer-free planar halide perovskite thin-film solar cells," *Nat. Commun.* **6**, 6700 (2015).

172. G. Sfyri et al., "Study of perovskite solar cells synthesized under ambient conditions and of the performance of small cell modules," *Sol. Energy Mater. Sol. Cells* **134**, 60–63 (2015).

173. A. D. Sheikh et al., "Atmospheric effects on the photovoltaic performance of hybrid perovskite solar cells," *Sol. Energy Mater. Sol. Cells* **137**, 6–14 (2015).

174. H. K. Raut et al., "Anti-reflective coatings: a critical, in-depth review," *Energy Environ. Sci.* **4**, 3779–3804 (2011).

175. H. J. Snaith, "Perovskites: the emergence of a new era for low-cost, high-efficiency solar cells," *J. Phys. Chem. Lett.* **4**, 3623–3630 (2013).

176. P. Löper et al., "Organic-inorganic halide perovskites : perspectives for silicon-based tandem solar cells," *J. Photovoltaics* **4**(6), 1545–1551 (2014).

177. B. W. Schneider et al., "Pyramidal surface textures for light trapping and antireflection in perovskite-on-silicon tandem solar cells," *Opt. Soc. Am.* **22**(October), 1422–1430 (2014).

178. A. J. M. Van Erven et al., "Gen5 production tool for light management textures," in *38th IEEE Photovoltaic Specialists Conf.*, IEEE, pp. 690–693 (2011).

179. H. J. Snaith et al., "SP: anomalous hysteresis in perovskite solar cells," *J. Phys. Chem. Lett.* **5**(9), 1511–1515 (2014).

180. E. L. Unger et al., "Hysteresis and transient behavior in current–voltage measurements of hybrid-perovskite absorber solar cells," *Energy Environ. Sci.* **7**(11), 3690–3698 (2014).

181. W. Tress et al., "Understanding the rate-dependent J-V hysteresis, slow time component, and aging in $CH_3NH_3PbI_3$ perovskite solar cells: the role of a compensated electric fiel," *RSC Adv.* **8**, 995–1004 (2015).

182. M. T. Neukom et al., "Why perovskite solar cells with high efficiency show small IV-curve hysteresis," *Sol. Energy Mater. Sol. Cells* **169**(November), 159–166 (2017).

183. Q. Wu et al., "Kesterite Cu_2ZnSnS_4 as a low-cost inorganic hole-transporting material for high-efficiency perovskite solar cells," *ACS Appl. Mater. Interfaces* **7**(51), 28466–28473 (2015).

184. G. A. Sepalage et al., "Copper(I) Iodide as hole-conductor in planar perovskite solar cells: probing the origin of J-V hysteresis," *Adv. Funct. Mater.* **25**(35), 5650–5661 (2015).

185. E. Erdenebileg et al., "Very small inverted hysteresis in vacuum-deposited mixed organic–inorganic hybrid perovskite solar cells," *Energy Technol.* **5**(9), 1606–1611 (2017).

186. F. Wu et al., "Bias-dependent normal and inverted J–V hysteresis in perovskite solar cells," *ACS Appl. Mater. Interfaces* **10**(30), 25604–25613 (2018).

187. F. Wu et al., "Inverted current–voltage hysteresis in perovskite solar cells," *ACS Energy Lett.* **3**(10), 2457–2460 (2018).

188. Y. Shao et al., "Origin and elimination of photocurrent hysteresis by fullerene passivation in $CH_3NH_3PbI_3$ planar heterojunction solar cells," *Nat. Commun.* **5**, 5784 (2014).

189. Y. Hishikawa et al., "Precise performance characterization of perovskite solar cells," *Curr. Appl. Phys.* **16**(8), 898–904 (2016).

190. H.-S. Kim et al., "Control of I-V hysteresis in $CH_3NH_3PbI_3$ perovskite solar cell," *J. Phys. Chem. Lett.* **6**(22), 4633–4639 (2015).

191. E. T. Hoke et al., "Reversible photo-induced trap formation in mixed-halide hybrid perovskites for photovoltaics," *Chem. Sci.* **6**(1), 613–617 (2015).
192. E. J. Juarez-Perez et al., "Photoinduced giant dielectric constant in lead halide perovskite solar cells," *J. Phys. Chem. Lett.* **5**(13), 2390–2394 (2014).
193. X. Y. Chin et al., "Lead iodide perovskite light-emitting field-effect transistor," *Nat. Commun.* **6**(May), 7383 (2015).
194. C. Eames et al., "Ionic transport in hybrid lead iodide perovskite solar cells," *Nat. Commun.* **6**(May), 7497 (2015).
195. N. Pellet et al., "Mixed-organic-cation perovskite photovoltaics for enhanced solar-light harvesting," *Angew. Int. Ed. Chem.* **53**(12), 3151–3157 (2014).
196. Y. Shao et al., "Grain boundary dominated ion migration in polycrystalline organic–inorganic halide perovskite films," *Energy Environ. Sci.* **9**(5), 1752–1759 (2016).
197. J. M. Frost et al., "Atomistic origins of high-performanc in hybrid halide perovskite solar cells.," *Nano Lett.* **14**(5), 2584–2590 (2014).
198. R. J. Sutton et al., "Bandgap-tunable cesium lead halide perovskites with high thermal stability for efficient solar cells," *Adv. Energy Mater.* **6**(8), 1502458 (2016).
199. N. Agmon, "The Grotthuss mechanism," *Chem. Phys. Lett.* **244**(5–6), 456–462 (1995).
200. J. A. Christians, P. A. Miranda Herrera, and P. V. Kamat, "Transformation of the excited state and photovoltaic efficiency of $CH_3NH_3PbI_3$ perovskite upon controlled exposure to humidified air," *J. Am. Chem. Soc.* **137**(4), 1530–1538 (2015).
201. S. de Wolf et al., "Organometallic halide perovskites: sharp optical absorption edge and its relation to photovoltaic performance," *J. Phys. Chem. C* **5**, 1035–1139 (2014).
202. J. Yang et al., "Investigation of $CH_3NH_3PbI_3$ degradation rates and mechanisms in controlled humidity environments using in situ techniques," *ACS Nano* **9**(2), 1955–1963 (2015).
203. B. David"Synthesis, structure, and properties of organic inorganic perovskites and related," in Progress in Inorganic Chemistry **96**, p. 1, John Wiley & Sons (2009).
204. W. Li et al., "Montmorillonite as bifunctional buffer layer material for hybrid perovskite solar cells with protection from corrosion and retarding recombination," *J. Mater. Chem. A* **2**(33), 13587–13592 (2014).
205. T. Leijtens et al., "Hydrophobic organic hole transporters for improved moisture resistance in metal halide perovskite solar cells," *ACS Appl. Mater. Interfaces* **8**(9), 5981–5989 (2016).
206. Y. Rong et al., "Hole-conductor-free mesoscopic $TiO_2/CH_3NH_3PbI_3$ heterojunction solar cells based on anatase nanosheets and carbon counter electrodes," *J. Phys. Chem. Lett.* **5**(12), 2160–2164 (2014).
207. X. Li et al., "Outdoor performance and stability under elevated temperatures and long-term light soaking of triple-layer mesoporous perovskite photovoltaics," *Energy Technol.* **3**(6), 551–555 (2015).
208. X. Xu et al., "Hole selective NiO contact for efficient perovskite solar cells with carbon electrode," *Nano Lett.* **15**(4), 2402–2408 (2015).
209. F. Zhang, "Structure engineering of hole–conductor free perovskite based solar cells with low temperature processed commercial carbon paste as cathode," *ACS Appl. Mater. Interfaces* **6**(18), 16140–16146 (2014).
210. D. Thrithamarassery Gangadharan et al., "Aromatic alkylammonium spacer cations for efficient two-dimensional perovskite solar cells with enhanced moisture and thermal stability," *Sol. RRL* **2**(4), 1700215 (2018).
211. K. Yao et al., "Multilayered perovskite materials based on polymeric-ammonium cations for stable large-area solar cell," *Chem. Mater.* **28**(9), 3131–3138 (2016).
212. L. N. Quan et al., "Ligand-stabilized reduced-dimensionality perovskites," *J. Am. Chem. Soc.* **138**(8), 2649–2655 (2016).
213. D. H. Cao et al., "2D Homologous perovskites as light-absorbing materials for solar cell applications," *J. Am. Chem. Soc.* **137**(24), 7843–7850 (2015).
214. A. Gheno et al., "Printable WO_3 electron transporting layer for perovskite solar cells: influence on device performance and stability," *Sol. Energy Mater. Sol. Cells* **161**, 347–354 (2017).

215. S. Ito et al., "Effects of surface blocking layer of Sb_2S_3 on nanocrystalline TiO_2 for $CH_3NH_3PbI_3$ perovskite solar cells," *J. Phys. Chem. C* **118**(30), 16995–17000 (2014).

216. A. Gheno et al., "Stability assessments on luminescent down-shifting molecules for UV-protection of perovskite solar cells," *Opt. Mater. (Amst).* **75**, 781–786 (2018).

217. B. K. Benavides-Garcia, "Bond energies, ionization potentials and the singlet-triplet energy separations of $SnCl_2$, $SnBr_2$, SnI_2, $PbCl_2$, $PbBr_2$, PbI_2, and their positive ions," *Chem. Phys.* **100**(4), 2821–2830 (1994).

218. K. W. Tan et al., "Thermally induced structural evolution and performance of mesoporous block copolymer-directed alumina perovskite solar cells," *ACS Nano* **8**(5), 4730–4739 (2014).

219. S. Aharon et al., "Temperature dependence of hole conductor free formamidinium lead iodide perovskite based solar cells," *J. Mater. Chem. A* **3**(17), 9171–9178 (2015).

220. L. Hu et al., "Investigation of the interaction between perovskite films with moisture via in situ electrical resistance measurement," *ACS Appl. Mater. Interfaces* **7**(45), 25113–25120 (2015)

221. B. Philippe et al., "Chemical and electronic structure characterization of lead halide perovskites and stability behavior under different exposures—a photoelectron spectroscopy investigation," *Chem. Mater.* **27**(5), 1720–1731 (2015).

222. Q. Hu et al., "Engineering of Electron-selective contact for perovskite solar cells with efficiency exceeding 15%," *ACS Nano* **8**(10), 10161–10167 (2014).

223. J. Yang et al., "Origin of the thermal instability in $CH_3NH_3PbI_3$ thin films deposited on ZnO," *Chem. Mater.* **27**(12), 4229–4236 (2015).

224. T. Supasai et al., "Formation of a passivating $CH_3NH_3PbI_3$/PbI_2 interface during moderate heating of CH 3NH3PbI3 layers," *Appl. Phys. Lett.* **103**(18), 183906 (2013).

225. P. Pistor et al., "Monitoring the phase formation of coevaporated lead halide perovskite thin films by in situ x-ray diffraction," *J. Phys. Chem. Lett.* **5**(19), 3308–3312 (2014).

226. T. Malinauskas et al., "Enhancing thermal stability and lifetime of solid-state dye-sensitized solar cells via molecular engineering of the hole-transporting material spiro-OMeTAD," *ACS Appl. Mater. Interfaces* **7**(21), 11107–11116 (2015).

227. K. Rakstys et al., "Triazatruxene-based hole transporting materials for highly efficient perovskite solar cells," *J. Am. Chem. Soc.* **137**(51), 16172–16178 (2015).

228. F. Zhang, D. H. Kim, and K. Zhu, "3D/2D multidimensional perovskites: balance of high performance and stability for perovskite solar cells," *Curr. Opin. Electrochem.* **11**, 105–113 (2018).

229. N. Adhikari et al., "Interfacial study to suppress charge carrier recombination for high efficiency perovskite solar cells," *ACS Appl. Mater. Interfaces* **7**(48), 26445–26454 (2015).

230. A. B. Muñoz-García and M. Pavone, "First-principles design of new electrodes for proton-conducting solid-oxide electrochemical cells: a-site doped $Sr_2Fe_{1.5}Mo_{0.5}O_6$-δ perovskite," *Chem. Mater.* **28**(2), 490–500 (2016).

231. Y. H. Kim et al., "Effects of thermal treatment on organic-inorganic hybrid perovskite films and luminous efficiency of light-emitting diodes," *Curr. Appl. Phys.* **16**(9), 1069–1074 (2016).

232. A. Dubey et al., "Room temperature{, } air crystallized perovskite film for high performance solar cells," *J. Mater. Chem. A* **4**(26), 10231–10240 (2016).

233. H. Zhou et al., "Interface engineering of highly efficient perovskite solar cells," *Science* **345**(6196), 542–546 (2014).

234. J. W. Lee et al., "Formamidinium and cesium hybridization for photo- and moisture-stable perovskite solar cell," *Adv. Energy Mater.* **5**(20), 1501310 (2015).

235. F. J. Ramos et al., "Fabrication and encapsulation of perovskites sensitized solid state solar cells," in *IEEE 40th Photovoltaic Specialist Conf. (PVSC)*, pp. 2584–2587 (2014).

236. F. C. Krebs, "Encapsulation of polymer photovoltaic prototypes," *Sol. Energy Mater. Sol. Cells* **90**(20), 3633–3643 (2006).

237. J. Lewis, "Material challenge for flexible organic devices," *Mater. Today* **9**(4), 38–45 (2006).

238. S. Schuller et al., "Determination of the degradation constant of bulk heterojunction solar cells by accelerated lifetime measurements," *Appl. Phys. A Mater. Sci. Process.* **79**(1), 37–40 (2004).

239. C. J. Brabec et al., "Polymer-fullerene bulk-heterojunction solar cells," *Adv. Mater.* **22**(34), 3839–3856 (2010).

240. M. Jørgensen, K. Norrman, and F. C. Krebs, "Stability/degradation of polymer solar cells," *Sol. Energy Mater. Sol. Cells* **92**(7), 686–714 (2008).

241. F. C. Krebs and H. Spanggaard, "Significant improvement of polymer solar cell stability," *Chem. Mater.* **17**(21), 5235–5237 (2005).

242. W. Tress et al., "Predicting the open-circuit voltage of $CH_3NH_3PbI_3$ perovskite solar cells using electroluminescence and photovoltaic quantum efficiency spectra: the role of radiative and non-radiative recombination," *Adv. Energy Mater.* **5**(3), 1400812 (2015).

243. L. Gil-Escrig et al., "Efficient photovoltaic and electroluminescent perovskite devices," *Chem. Commun.* **51**(3), 569–571 (2015).

244. N. Dubey et al., "Interfacial study to suppress charge carrier recombination for high efficiency perovskite solar cells," *ACS Appl. Mater. Interfaces* **7**(48), 26445–26454 (2015).

245. Y. Li, K. S. Moon, and C. P. Wong, "Electronics without lead," *Science* **308**(5727), 1419–1420 (2005).

246. V. I. Slaveykova and K. J. Wilkinson, "Physicochemical aspects of lead bioaccumulation by *Chlorella vulgaris*," *Environ. Sci. Technol.* **36**(5), 969–975 (2002).

247. L. Whitzling, M. Wander, and E. Phillips, "Testing and educating on urban soil lead: a case of Chicago community gardens," *J. Agric. Food Syst. Community Dev.* **1**(2), 167–185 (2010).

248. F. R. Stoddard, II et al., "Iodine alters gene expression in the MCF7 breast cancer cell line : evidence for an anti-estrogen effect of iodine," *Int. J. Med. Sci.* **5**(4), 189–196 (2008).

249. T. T. Sherer, K. D. Thrall, and R. J. Bull, "Comparison of toxicity induced by iodine and iodide in male and female rats," *J. Toxicol. Environ. Health* **32**(1), 89–101 (1991).

250. M. Mayer et al., "Different transport mechanisms in plant and human AMT/Rh-type ammonium transporters," *J. Gen. Physiol.* **127**(2), 133–144 (2006).

251. H. Needleman, "Lead poisoning," *Annu. Rev. Med.* **55**, 209–222 (2004).

252. D. Cortecchia et al., "Lead-Free $MA_2CuCl_xBr_{4-x}$ hybrid perovskites," *Inorg. Chem.* **55**(3), 1044–1052 (2016).

253. T. Yokoyama et al., "The origin of lower hole carrier concentration in methylammonium tin halide films grown by a vapor-assisted solution process," *ACS Energy Lett.* **2**(1), 22–28 (2016).

254. C.-M. Tsai et al., "Role of tin chloride in tin-rich mixed-halide perovskites applied as mesoscopic solar cells with a carbon counter electrode," *ACS Energy Lett.* **1**(6), 1086–1093, (2016).

255. A. Wang et al., "Controlled synthesis of lead-free and stable perovskite derivative Cs_2SnI_6 nanocrystals via a facile hot-injection process," *Chem. Mater.* **28**(22), 8132–8140 (2016).

256. S. Gupta et al., "$CsSnBr_3$, a lead-free halide perovskite for long-term solar cell application: insights on SnF_2 addition," *ACS Energy Lett.* **1**(5), 1028–1033 (2016).

257. L.-J. Chen et al., "Synthesis and optical properties of lead-free cesium tin halide perovskite quantum rods with high-performance solar cell application," *J. Phys. Chem. Lett.* **7**(24), 5028–5035 (2016).

258. W. Zhang et al., "Triiodide-induced band-edge reconstruction of a lead-free perovskite-derivative hybrid for strong light absorption," *Chem. Mater.* **30**, 4081–4088 (2018).

259. T. Yokoyama et al., "Overcoming short-circuit in lead-free $CH_3NH_3SnI_3$ perovskite solar cells via kinetically controlled gas–solid reaction film fabrication process," *J. Phys. Chem. Lett.* **7**(5), 776–782 (2016).

260. G. Volonakis et al., "Lead-free halide double perovskites via heterovalent substitution of noble metals," *J. Phys. Chem. Lett.* **7**(7), 1254–1259 (2016).

261. G. Volonakis et al., "Cs2InAgCl6: a new lead-free halide double perovskite with direct band gap," *J. Phys. Chem. Lett.* **8**(4), 772–778 (2017).

262. F. Wei et al., "Synthesis and properties of a lead-free hybrid double perovskite: $(CH_3NH_3)_2AgBiBr_6$," *Chem. Mater.* **29**(3), 1089–1094 (2017).

263. H. C. Sansom et al., "AgBiI4 as a lead-free solar absorber with potential application in photovoltaics," *Chem. Mater.* **29**(4), 1538–1549 (2017).

264. I. C. Smith et al., "A layered hybrid perovskite solar-cell absorber with enhanced moisture stability," *Angew. Chem.* **126**, 11414–11417 (2014).

265. M. G. Kanatzidis, "2D homologous perovskites as light-absorbing materials for solar cell applications," *J. Am. Chem. Soc.* **2**(137), 7843–7850 (2015).
266. I. Zimmermann et al., "One-year stable perovskite solar cells by 2D/3D interface engineering," *Nat. Commun.* **8**, 15684 (2017).
267. N. K. Kumawat et al., "Structural, optical, and electronic properties of wide bandgap perovskites: experimental and theoretical investigations," *J. Phys. Chem. A* **120**(22), 3917–3923 (2016).
268. A. D. Jodlowski et al., "Large guanidinium cation mixed with methylammonium in lead iodide perovskites for 19% efficient solar cells," *Nat. Energy* **2**(12), 972–979 (2017).
269. A. Z. Chen et al., "Origin of vertical orientation in two-dimensional metal halide perovskites and its effect on photovoltaic performance," *Nat. Commun.* **9**(1), 1336 (2018).

Unni Krishnan is a PhD student in the Department of Nanotechnology at Sri Guru Granth Sahib World University (SGGSWU). He received his MTech degree in aerospace from Defence Institute of Armament Technology, Pune, India, in 2013. His current research interest includes semiconducting nanoparticle and their application.

Manjot Kaur is a PhD student in the Department of Nanotechnology at SGGSWU. She has completed her MTech degree with a gold medal in 2018. Her research interest includes development of innovative nanomaterial for semiconducting and biomedical applications.

Manjeet Kumar is a postdoctoral fellow at Incheon National University. He received his PhD from the DIAT-DRDO, Pune, India, in 2016. He completed his MTech degree in 2009 from Thapar University. From 2009 to 2010, he worked as a project associate at IIT, Delhi, India. His research interest includes chemical and physical processing of metal oxides, such as nanowires and functional thin/thick films for sensing applications, and study of interaction mechanism at gas–solid interfaces.

Akshay Kumar is an assistant professor in the Department of Nanotechnology at SGGSWU, India. He received his doctoral degree from Thapar University, India, in 2011, and master's degree in applied physics from Punjabi University in 2005. He is the author and coauthor of more than 50 research papers and has written one book. His research interest includes structure property relation of nanostructured materials.